J. Fluid Mech. (2024), *vol*. 978, A1, doi:10.1017/jfm.2023.926

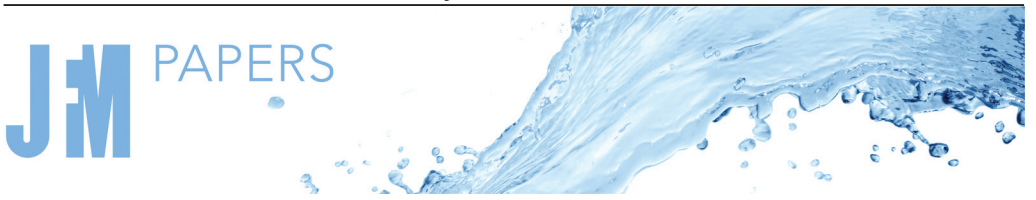

The role of viscoplastic drop shape in impact

Kindness Isukwem[1], Julie Godefroid[2], Cécile Monteux[2], David Bouttes[3], Romain Castellani[1], Elie Hachem[1], Rudy Valette[1] and Anselmo Pereira[1],†

[1]Mines Paris, PSL University, Centre for material forming (CEMEF), UMR CNRS 7635, rue Claude Daunesse, 06904 Sophia-Antipolis, France

[2]Sciences et Ingénierie de la Matière Molle, ESPCI Paris, PSL Research University, UMR CNRS 7615, Sorbonne Université, Paris, France

[3]Saint-Gobain CREE, 550 rue Alphonse Jauffret, Cavaillon 84300, France

(Received 25 January 2023; revised 17 October 2023; accepted 19 October 2023)

The impact of fluid drops on solid substrates is a cardinal fluid dynamics phenomenon intrinsically related to many fields. Although these impacting objects are very often non-spherical and non-Newtonian, previous studies have mainly focused on spherical Newtonian drops. As a result, both shape and rheological effects on the drop-spreading dynamics remain largely unexplored. In the present work we use a mixed approach combining experiments with multiphase three-dimensional numerical simulations to extend the work reported by Luu & Forterre (*J. Fluid Mech.*, vol. 632, 2009, pp. 301–327) by highlighting the fundamental role of shape in the normal impact of viscoplastic drops. Such complex fluids are highly common in various industrial domains and ideally behave either like a rigid body or a shear-rate-dependent liquid, according to the stress solicitation. Spherical, prolate, cylindrical and prismatic drops are considered. The results show that, under negligible capillary effects, the impacting kinetic energy of the drop is dissipated through viscoplastic effects during the spreading process, giving rise to three flow regimes: (i) inertio-viscous, (ii) inertio-plastic, and (iii) mixed inertio-visco-plastic. These regimes are deeply affected by the drop initial aspect ratio, which in turn reveals the possibility of using drop shape to control spreading. The physical mechanisms driving the considered phenomenon are underlined by energy budget analyses and scaling laws. The results are summarised in a two-dimensional diagram linking the drop maximum spreading, minimum height and final shape with different spreading regimes through a single dimensionless parameter, here called the impact number.

Key words: drops, multiphase flow, plastic materials

† Email address for correspondence: anselmo.soeiro_pereira@mines-paristech.fr

1. Introduction

The spreading of drops impacting hydrophobic surfaces is a paramount fluid mechanics phenomenon (Worthington 1883; Rein 1993), which occurs in a large number of areas from inkjet-based bioprinting of cells, tissues and organs (Murphy & Atala 2020; Yumoto *et al.* 2020) to the production of capsules, beads and non-spherical particles resulting from the polymerisation of droplets through a liquid–air interface (Godefroid 2019), raindrops and pesticide deposition (Yarin 2006), coating (Andrade, Osorio & Skurtys 2013) and firefighting (Josserand & Thoroddsen 2016). In some of these processes, fluid drops tend to behave as viscoplastic materials: at lower stress levels, they act like a non-deformable solid and at stress levels higher than the characteristic yield stress τ_0, they deform like a complex (non-Newtonian) liquid (Balmforth, Frigaard & Ovarlez 2014; Thompson & Soares 2016; Jalaal, Kemper & Lohse 2019; Valette *et al.* 2021). More specifically, some of the microstructural interactions developed in these materials (intermolecular attractive and/or repulsive forces, friction, capillary bridges, among others) are translated at the macroscopic level through a yield-stress and a strain-rate-dependent viscosity η. The latter is commonly represented by the Herschel–Bulkley viscosity equation (only valid for flowing regions; Herschel & Bulkley 1926) according to which $\eta = k|\,\dot{\boldsymbol{\gamma}}\,|^{m-1} + \tau_0/|\,\dot{\boldsymbol{\gamma}}\,|$, where k is the consistency index, m is the flow index and $|\,\dot{\boldsymbol{\gamma}}\,|$ is the norm of the strain-rate tensor. The list of materials that can exhibit such a behaviour includes mineral dense suspensions (bentonite, kaolin, carbon black, toothpaste and granular suspensions; Luu & Forterre 2009; Guazzelli & Pouliquen 2018; Dages *et al.* 2021; Ness, Seto & Mari 2022), organic suspensions (Carbopol-based microgels, alginate suspensions, ketchup; Balmforth *et al.* 2014; Godefroid 2019; Jalaal *et al.* 2019), emulsions (mayonnaise; Zhang & Makse 2005; Derkach 2009; Tenorio-Garcia *et al.* 2022) and foams (Cohen-Addad, Reinhard & Pitois 2013).

In contrast with Newtonian impacting drops (Yarin 2006; Josserand & Thoroddsen 2016), very few studies have been reported on the impact of viscoplastic drops (German & Bertola 2009; Luu & Forterre 2009; Kim & Baek 2012; Luu & Forterre 2014; Blackwell *et al.* 2015; Oishi, Thompson & Martins 2019; Jørgensen, Forterre & Lhuissier 2020; Sen, Morales & Ewoldt 2020), which emerges from their complex nature. Some of the differences between Newtonian and viscoplastic impact scenarios are illustrated in figure 1, where experimental snapshots show the spreading evolution of a water drop (figure 1*a*), as well as bentonite-in-water drops at three particle mass fractions ϕ: 0.5 (figure 1*b*), 0.55 (figure 1*c*) and 0.6 (figure 1*d*). The drops fall freely from a 5 mm diameter nozzle, hitting a hydrophilic acrylic plate (Quetzeri-Santiago *et al.* 2019) at an impact velocity U_0 of 1.25 m s^{-1}. As ϕ increases, 5 µm mineral particles aggregate in house-of-cards-like clusters mainly through electrostatic and Van der Waals interactions (Chafe & Bruyn 2005), building a microstructure that leads ultimately to the appearance of an increasing macroscopic yield stress of 5 Pa, 50 Pa and 500 Pa, respectively. As τ_0 increases, the material resistance to surface-tension-induced deformations during the free fall becomes more pronounced. Consequently, its initial shape moves from spherical/quasi-spherical (figure 1*a*,*b*) to prolate-like (figure 1*c*,*d*) characterised not only by an initial diameter D_0 of 5 mm imposed by the nozzle, but also by an initial height H_0 of 12.5 mm. During the spreading process, the impacting kinetic energy is partially converted into surface energy, and partially dissipated by viscoplastic effects until the drop reaches its maximum spreading D_{max} and minimum height H_{min} at the instant t_{max}. Kelvin–Helmholtz instabilities induced by liquid–air interactions (Liu *et al.* 2021) at low ϕ tend to be suppressed by dissipative effects at larger τ_0, while D_{max} decreases. At $\tau_0 = 500$ Pa, the drop exhibits the lowest final spreading level and preserves its top portion,

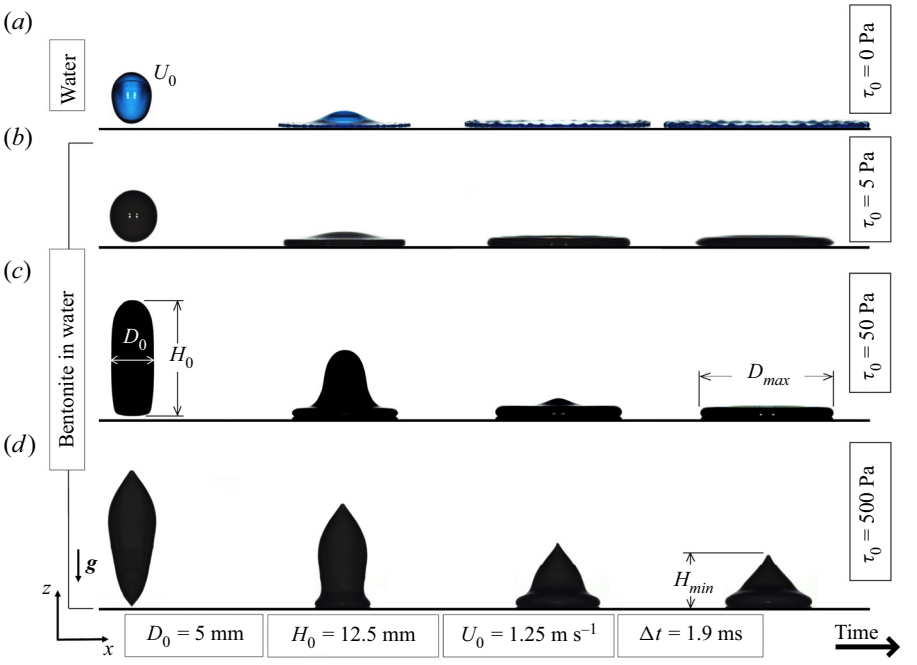

Figure 1. Experimental snapshots showing the spreading evolution of a water drop (*a*) and bentonite-in-water drops at three particle mass fractions ϕ (*b–d*). The yield stress τ_0 increases with ϕ: (*a*) $\phi = 0$, $\tau_0 = 0$ Pa; (*b*) $\phi = 0.5$, $\tau_0 = 5$ Pa; (*c*) $\phi = 0.55$, $\tau_0 = 50$ Pa; and (*d*) $\phi = 0.6$, $\tau_0 = 500$ Pa. The impact velocity is $U_0 = 1.25$ m s^{-1}. The diameter of the drops is $D_0 = 5$ mm, and the height of the prolate ones is $H_0 = 12.5$ mm. The interval Δt between two images is 1.9 ms.

i.e. its bottom part spreads like a viscous liquid, while its upper portion tends to behave like a solid. In these connections, an open issue arises: can one predict D_{max}, H_{min} and t_{max} for viscoplastic non-spherical impacting drops? This question is addressed in the present work.

The very few studies on impacting viscoplastic drops conducted up to now (Luu & Forterre 2009; Oishi *et al.* 2019) specify that, under negligible surface tension effects, the maximum relative spreading D_{max}/D_0 depends on two dimensionless parameters: the diameter-*m*-based Reynolds number defined for a Herschel–Bulkley fluid as $Re_{m,D} = \rho U_0^2/k(U_0/D_0)^m$ (the ratio of the kinetic to the viscous stress) and the plastic number defined as $Pl = \tau_0/\rho U_0^2$ (the ratio of the yield stress to the kinetic stress). More precisely, according to those studies, each $Re_{m,D} - Pl$ couple induces a unique D_{max}/D_0 regardless of the volume of the impacting object. This idea is experimentally explored in figure 2, where snapshots illustrate the spreading of three bentonite-in-water drops impacting a hydrophilic acrylic plate at $Re_{m,D} = 47$ and $Pl = 0.18$. In agreement with the reported theoretical arguments, both the top-line and middle-line drops exhibit similar spreading evolutions with a maximum relative spreading D_{max}/D_0 of 1.24, although their volumes differ. However, when increasing the volume of the middle-line drop through a simple height enhancement (see figure 2(*c*) for which $H_0/D_0 = 4$), one observes a distinct spreading dynamics with $D_{max}/D_0 = 1.91$. Such differences indicate that H_0/D_0 also plays a relevant role in the spreading dynamics, an effect not considered by the current theory (Luu & Forterre 2009). Note that aspect ratio effects are also observed when defining the Reynolds number based on the initial height of the drop, $Re_{m,H} = \rho U_0^2/k(U_0/H_0)^m$ (height-*m*-based Reynolds number), a result shown by figure 3,

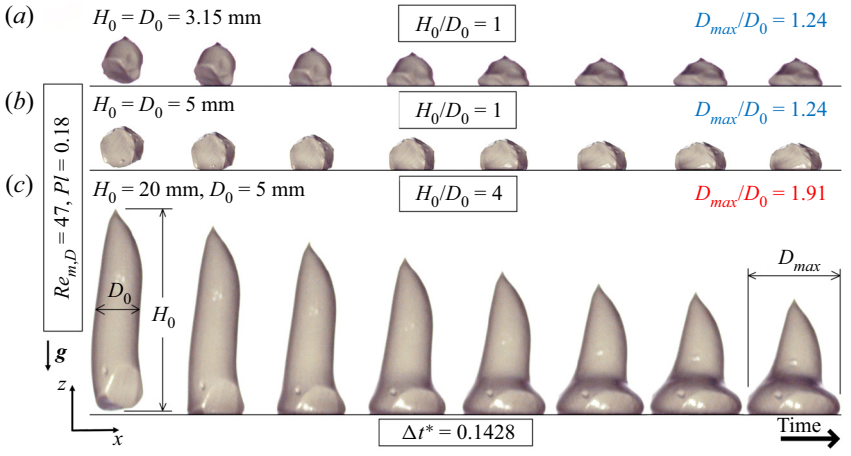

Figure 2. Experimental snapshots illustrating the spreading time evolution of three bentonite-in-water drops impacting a hydrophilic acrylic plate at $Re_{m,D} = 47$ and $Pl = 0.18$. The dimensionless interval $\Delta t^* = t/t_{max}$ between two images is 0.1428 (t_{max} being the instant at which the drop achieves its maximum spreading D_{max}). Clearly, regardless of the volume of the drop V_{total}, D_{max}/D_0 is an increasing function of H_0/D_0: (*a*) $V_{total} = 1.64 \times 10^{-8}$ m^3, $H_0/D_0 = 1$, $D_{max}/D_0 = 1.24$; (*b*) $V_{total} = 6.54 \times 10^{-8}$ m^3, $H_0/D_0 = 1$, $D_{max}/D_0 = 1.24$; (*c*) $V_{total} = 2.62 \times 10^{-7}$ m^3, $H_0/D_0 = 4$, $D_{max}/D_0 = 1.91$.

where mayonnaise drops with distinct H_0/D_0 impacting an acrylic plate at the same $Re_{m,H} - Pl$ exhibit different D_{max}/D_0.

In this work, we highlight the fundamental role of viscoplastic drop shape in normal impact. More specifically, we extend the seminal work of Luu & Forterre (2009) by analysing the drop initial aspect ratio effect on the spreading dynamics, maximum spreading, minimum height and spreading time of viscoplastic non-spherical drops impacting a solid hydrophilic surface. Our study is conducted through a mixed approach combining three-dimensional (3-D) numerical simulations and experiments. Numerical simulations based on an adaptive variational multi-scale method for two materials (viscoplastic drop and air) are performed and compared with experiments. The latter are either taken from existing literature or carried out with various yield-stress materials, such as Carbopol-based microgels, alginate suspensions, bentonite and kaolin colloidal suspensions, mayonnaise and ketchup. The results are explored in light of energy budget analyses and scaling laws, which stress the investigated problem's physical mechanisms. Lastly, they are summarised in a two-dimensional diagram linking the maximum diameter, minimum height and final shape of the drops with different flow spreading regimes through a single dimensionless parameter called here the impact number, the latter being a function of $Re_{m,D}$, Pl and H_0/D_0.

The organization of the paper is as follows. A detailed description of the physical formulation and the mixed experimental–numerical method is presented in § 2. Experimental/numerical results are discussed in § 3. Finally, conclusions and perspectives are drawn in the closing section.

2. Problem statement: experimental and numerical viscoplastic non-spherical drop impact on a solid

As illustrated in figures 1, 2 and 3, we consider both experimentally and numerically the normal impact of viscoplastic Herschel–Bulkley falling drops of initial diameter D_0,

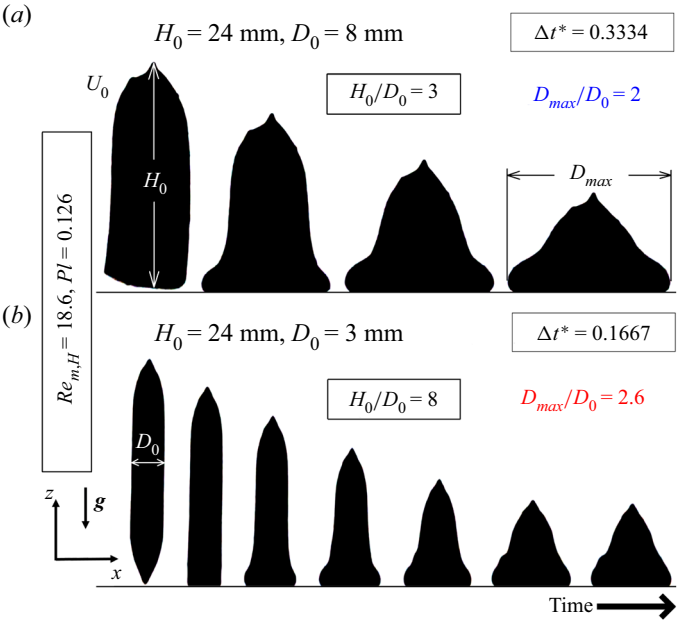

Figure 3. Experimental snapshots showing the spreading evolution of two prolate mayonnaise drops impacting an acrylic plate at $Re_{m,H} = 18.6$ and $Pl = 0.126$. The dimensionless interval $\Delta t^* = t/t_{max}$ between two images is 0.3334 for the upper-line case, and 0.1667 ms for the bottom-line case. As observed, different initial aspect ratios induce distinct maximum relative spreading: (*a*) $H_0/D_0 = 3$, $D_{max}/D_0 = 2$; (*b*) $H_0/D_0 = 8$, $D_{max}/D_0 = 2.6$.

initial height H_0, density ρ, consistency k, flow index m and yield stress τ_0 against a hydrophilic plate. The drop hits the plate at the instant t_0 exhibiting an impact velocity U_0. It then spreads radially, undergoing shear and wetting the solid surface before achieving a maximum diameter D_{max} and a minimum height H_{min} at the instant t_{max}. The eventual retraction of the drop induced by surface tension effects is not considered here. Splashing events are not taken into account either (Peters, Xu & Jaeger 2013; Blackwell *et al.* 2015; Josserand & Thoroddsen 2016). The drop and the plate are surrounded by air whose density is ρ_{air} and viscosity is η_{air}. Surface tension between the different phases of the system is denoted by σ.

The drop behaviour is described only through gravitational, inertial, capillary and viscoplastic Herschel–Bulkley parameters. Nevertheless, we show that such physical ingredients are sufficient to capture the main features observed in our experiments.

The important dimensionless quantities of the problem Π_i can be stressed by a classical dimensional analysis based on the Buckingham-Π theorem with the following dimensional variables H_0, D_0, U_0, g, ρ, k, m, τ_0 and σ. By doing so, one finds that

$$\Pi_1 = \frac{H_0}{D_0}, \quad \Pi_2 = \frac{k\,(U_0/D_0)^m}{\rho U_0^2}, \quad \Pi_3 = \frac{\tau_0}{\rho U_0^2}, \quad \Pi_4 = \frac{\rho g D_0}{\rho U_0^2}, \quad \text{and} \quad \Pi_5 = \frac{\sigma/D_0}{\rho U_0^2}, \tag{2.1a–e}$$

where $\Pi_2 = 1/Re_{m,D}$, $\Pi_3 = Pl$, $\Pi_4 = 1/Fr$ (in which Fr is the Froude number) and $\Pi_5 = 1/We$ (where We is the Weber number). Since we consider here centimetric/millimetric drops for which k and/or τ_0 are/is relatively high, $\rho g D_0$ and σ/D_0 end up playing a marginal role in comparison to the other stress terms, i.e. $\Pi_4 \leq 0.1$

and $\Pi_5 \leq 0.01$ (this will be shown in detail in the following subsection). This particular problem can be explored with the first three dimensionless parameters listed above: H_0/D_0, $Re_{m,D}$ and Pl.

Alternatively, the important dimensionless quantities of the problem can be stressed by assuming that both the impacting gravitational potential energy of the drop ($\sim \rho g H_0 (H_0 D_0^2)$), and its kinetic energy ($\sim \rho U_0^2 (H_0 D_0^2)$) are partially dissipated by viscoplastic effects (estimated at first glance as $\sim k(U_0/H_0)^m D_0^3 + \tau_0 D_0^3$), as well as partially converted into surface energy (approximated as $\sim(\sigma/D_0)(H_0 D_0^2)$ at this stage of the present work) during the spreading process

$$\rho g H_0 \left(H_0 D_0^2\right) + \rho U_0^2 \left(H_0 D_0^2\right) \sim k \left(\frac{U_0}{H_0}\right)^m D_0^3 + \tau_0 D_0^3 + \frac{\sigma}{D_0}\left(H_0 D_0^2\right) \tag{2.2}$$

(a better estimation of the right-hand side terms will be given in § 3). As underlined earlier, centimetric/millimetric drops for which k and/or τ_0 are/is relatively high (such as those used here) lead to marginal $\rho g H_0 (H_0 D_0^2)$ and $\rho g H_0 (H_0 D_0^2)$ in comparison to the other energy terms. Furthermore, in the present work $(k(U_0/H_0)^m + \tau_0)/(\sigma/D_0) > 10$ (a point detailed in the following subsection). Thus, the above equation is rewritten as

$$\rho U_0^2 \sim k \left(\frac{U_0}{D_0}\right)^m \left(\frac{D_0}{H_0}\right)^{m+1} + \tau_0 \left(\frac{D_0}{H_0}\right), \tag{2.3}$$

underlining that the impacting kinetic energy of the drop is mainly dissipated by both viscous and plastic effects during spreading. As a result, at least two spreading scenarios are expected to occur: inertio-viscous (balancing kinetic and viscous stresses) and inertio-plastic (balancing kinetic and yield stresses). By dividing the above equation by ρU_0^2 (driving stress), one finds that

$$1 \sim \frac{1}{Re}\frac{D_0}{H_0}, \tag{2.4}$$

in which Re is the Reynolds number (similar to Blackwell *et al.* 2015; Thompson, Sica & de Souza Mendes 2018; Sen *et al.* 2020). Clearly, (2.4) indicates that the drop spreading considered here is essentially a dissipative process exposed to shape effects. Finally, aiming to make our study directly comparable to the one conducted by Luu & Forterre (2009), the right-hand side term of the above equation is divided into

$$1 \sim \frac{1}{Re_{m,D}} \left(\frac{D_0}{H_0}\right)^{m+1} + Pl \left(\frac{D_0}{H_0}\right), \tag{2.5}$$

which underlines that the relevant dimensionless parameters of the problem are $Re_{m,D}$, Pl and H_0/D_0, as previously pointed out by Buckingham-Π-theorem-based analyses. Their effects on the spreading process will be highlighted in § 3.

2.1. *Experimental approach*

The experimental set-up for the investigation of the role of viscoplastic drop shape during impact is illustrated in figure 4. The viscoplastic drop of height H_0 and diameter D_0 falls by gravity $\boldsymbol{g}$ from a nozzle and hits the solid acrylic plate at the instant t_0 at an impact velocity U_0. The drop aspect ratio is imposed by controlling the fluid volume within the nozzle, while U_0 is a function of the distance between the nozzle and the plate

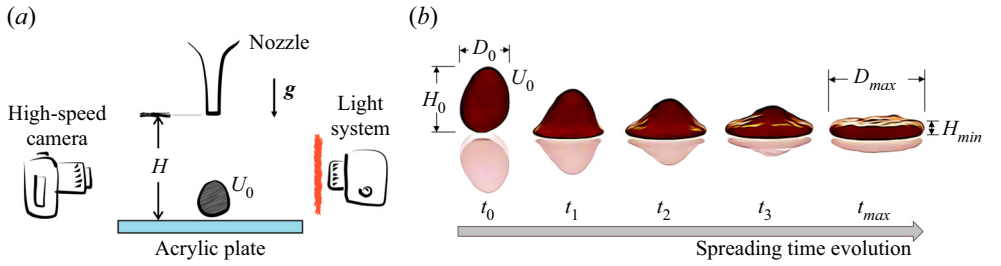

Figure 4. (*a*) Experimental set-up for the investigation of the role of viscoplastic drop shape in impact. The viscoplastic drop of height H_0 and diameter D_0 falls by gravity $\boldsymbol{g}$ from a nozzle and hits the solid acrylic plate at the instant t_0 at an impact velocity U_0 (U_0 being a function of the distance between the nozzle and the plate H; $U_0 \propto \sqrt{H}$). (*b*) After the impact, the drop spreads radially until it achieves a maximum diameter D_{max} and a minimum height H_{min} at the instant t_{max}. A ketchup drop is used for the illustrated impact event ($U_0 = 1.25$ m s^{-1}, $D_0 = 5$ mm, $H_0 = 7.5$ mm, $\rho = 1250$ kg m^{-3}, $k = 10$ Pa s^m, $m = 0.5$, $\tau_0 = 12$ Pa and $D_{max}/D_0 = 1.82$). It is recorded by a high-speed camera ($O(10^4)$ frames per second) with the aid of a LED backlight panel. A movie showing the mentioned impact event is available as a supplemental material at https://doi.org/10.1017/jfm.2023.926 (see supplementary movie 1).

H ($U_0 \propto \sqrt{H}$). Impact events are experimentally recorded by a Optronis Cyclone 2-2000 high-speed camera ($O(10^4)$ frames per second) equipped with a Sigma 105 mm F2.8 DG OS HSM macro lens, and with the aid of a LED backlight panel. Initial drop diameters D_0 are in the range of 2–20 mm, while the initial drop heights H_0 vary from 2 mm to 40 mm, and the impact velocities U_0 vary from 1 m s^{-1} to 4 m s^{-1}. The hydrophilic plate is acrylic (Quetzeri-Santiago *et al.* 2019). A variety of fluids are used: sodium alginate in 40 % by weight zirconia-in-deionized-water solutions (A); Carbopol-based microgels (C); 5 μm bentonite particles in deionized water (B-W); 5 μm bentonite particles in 50 % by weight glycerol-in-deionized-water solution (B-G-W); 5 μm kaolin particles in deionized water (K-W); Amora, Bénédicta and Hellmann's mayonnaises (M); and Amora, Nature and Heinz ketchups (K). Suspensions at different concentrations are prepared by following the procedures detailed in Luu & Forterre (2009) and Godefroid (2019).

Although the fluids listed above present a viscoplastic behaviour, they are of different natures and microstructures. This diversity allows for a variety of accessible yield stresses and flow behaviours (from viscoplastic to almost purely plastic suspensions). Mayonnaise (though in reality more complex than that) can be seen as an oil-in-water emulsion with micrometric-sized droplets (Ma & Barbosa-Cánovas 1995*a*,*b*; Derkach 2009). Ketchup is a tomato paste that can be seen as a organic suspension (Bottiglieri *et al.* 1991; Coussot & Gaulard 2005; Koocheki *et al.* 2009). Bentonite and kaolin in deionized water and in a glycerol-in-deionized-water solution, in turn, are clay suspensions made of micrometric sheet-like particles that interact between them thanks to van der Waals and electrostatic forces (Luu & Forterre 2009; Loisel *et al.* 2015; Mwasame, Wagner & Beris 2016; Vázquez-Quesada & Ellero 2016; Chun *et al.* 2017; Tanner 2018; Lin *et al.* 2019). They can form house-of-cards structures, since the electric charges of the edges and the centres of the particles are different (in both water and glycerol-in-water solution). Arrangements can become more complex, depending on ion concentration in solution and pH (forming aggregates, pillars or more homogeneous structures). Yield stress emerges from the network percolation and is also dependent on solid concentration. In addition, Carbopol microgels are crosslinked acrylic acid polymers that swell in water (Coussot 2007; Paiu 2007; Balmforth *et al.* 2014). Finally, the alginate suspensions are composed

of a charged biopolymer (alginate) and zirconia particles, which gives rise to a yield-stress fluid due to depletion interactions (Godefroid 2019).

Solid content, pH and ion concentration play an important role in the rheological parameters of the used fluids. Although we do not plan to discuss relationships between rheology and microstructure in the present work, it is worth mentioning that we do characterise the fresh materials just before the impact experiments to ensure the use of accurate rheological parameter values.

The used fluids are rheologically characterised using an ARES-G2 rheometer (TA Instruments) equipped with a cone-plate geometry. Their relevant properties and concentrations are listed in table 1. Experimental data available in the literature are also considered. As indicated by the yield stress and the storage modulus G' levels, these materials exhibit elasto-viscoplastic characteristics. Some of them are illustrated in figure 5 where the shear stress is displayed as a function of $|\dot{\boldsymbol{\gamma}}|$ (figure 5*a*), and G' is plotted as a function of the shear stress (figure 5*b*) for four samples: 57 % by weight bentonite-in-deionized-water (colloidal suspension; grey circles); 3 % by weight Carbopol microgel (polymers; blue triangles); Nature ketchup (organic suspension; red diamonds); and Amora mayonnaise (emulsion; green squares). However, except for the alginate drops, elasticity does not play a relevant role in the impact events studied here, which is underlined by comparing the estimated relaxation time λ of the considered materials ($\lambda \approx (k/G')^{1/m}$; Luu & Forterre 2009) to the flow characteristic time H_0/U_0, i.e. $De = (k/G')^{1/m}/(H_0/U_0) < 1$, where De is the Deborah number (we set specific values of H_0, D_0 and U_0 allowing De to keep lower than 1). Nevertheless, the alginate suspensions used here can be slightly exposed to elastic effects since, for these drops, $1.68 \leq De \leq 6.7$. Moreover, although some of the used fluids can be affected by further non-Newtonian signatures, such as microstructural orientation/anisotropy and thixotropy (their mechanical properties can evolve at rest; see the Appendix for a brief discussion on thixotropy; Pignon, Magnin & Piau 1996; Coussot 2005; Coussot *et al.* 2005; Paiu 2007; Balmforth, Forterre & Pouliquen 2009; Balmforth *et al.* 2014), none of these are taken into account given the size of our drops (millimetric/centimetric), the axisymmetric nature of the problem and its typical impact/spreading time scale (few ms; similar to Luu & Forterre 2009, 2014). Lastly, since most surface tension measurement methods are corrupted by the fluid yield stress and elasticity, we follow previous works (Luu & Forterre 2009; Jalaal *et al.* 2019) and take pure water surface tension as an upper bound for the real σ of our fluids, i.e. $\sigma < 0.072$ N m^{-1}. As a result, one can show that, for the flow cases analysed here, the ratio of the viscoplastic stress to the capillary stress is always greater than 10, i.e. $Ca = (k(U_0/H_0)^m + \tau_0)/(\sigma/D_0) > 10$, where Ca is the capillary number (except for alginate whose Ca is around 1). In other words, surface tension plays a marginal role (which will be shown in detail in § 3) when compared with viscoplastic effects. In these connections, we have also neglected any wetting phenomenon (such as hysteresis and dissipation at the contact line) that may particularly affect the receding dynamics (Richard, Clanet & Quéré 2002; de Gennes, Brochard-Wyart & Quéré 2005; Nigen 2005; Quéré 2008; Bonn *et al.* 2009; Duez *et al.* 2010; Carlson, Do-Quang & Amberg 2011).

2.2. *Numerical approach*

Our multiphase computational approach is based on a general solver (CIMLIB-CFD, a parallel, finite element library; Coupez & Hachem 2013) that takes into account the rheological behaviour of each fluid phase (viscoplastic drop and air; figure 6), as well as surface tension effects (Riber *et al.* 2016; Pereira *et al.* 2019; Valette *et al.* 2019; Pereira, Hachem & Valette 2020; Valette *et al.* 2021). More precisely, the momentum equation

https://doi.org/10.1017/jfm.2023.926 Published online by Cambridge University Press

Fluid	Weight (%)	ρ (kg m^{-3})	k (Pa s^m)	m	τ_0 (Pa)	$G'(\lvert\boldsymbol{\tau}\rvert \to 0)$ (Pa)	D_0 (mm)	H_0 (mm)	H_0/D_0	References
A	0.4	1010	0.1	0.79	0.3	9	2	2	1	Present work
C	0.1–4	1007–1020	1.5–35	0.5	2.5–150	30–1034	4–20	4–40	1–4	Present work
B-W	54–64	1050–1110	0.1–1	0.96–1	50–1250	952–400534	4–20	4–40	1–6	Present work
B-W	13–15	1090	0.12–0.16	0.96	68–124	2400–3800	14–27	14–27	1	Luu & Forterre (2009)
B-G-W	46–54	1050–1150	11–130	0.5	5.5–500	2830–109 500	4–20	4–40	1–5	Present work
K-W	47–53	1600–1640	5–25	0.38–0.5	15–240	34 000–620 000	4–20	4–40	1–4	Present work
K-W	51–55	1630	36–68	0.36	50–91	37 000–200 000	20–27	20–27	1	Luu & Forterre (2009)
M	* * *	965–980	10–50	0.32–0.45	30–125	133–5000	4–10	4–40	1–8	Present work
K	* * *	1170–1250	7.75–10	0.4	7–12	140–773	5–10	5–20	1–2.5	Present work

Table 1. Details concerning the considered fluids for the experiments: A = sodium alginate in 40 % by weight zirconia-in-deionized-water solutions; C = Carbopol-based microgels; B-W = 5 μm bentonite particles in deionized water; B-G-W = 5 μm bentonite particles in 50 % by weight glycerol-in-deionized-water solution; K-W = 5 μm kaolin particles in deionized water; M = Amora, Bénédicta and Hellmann's mayonnaises; K = Amora, Nature and Heinz ketchups. Impact velocities U_0 vary from 1 m s^{-1} to 4 m s^{-1}.

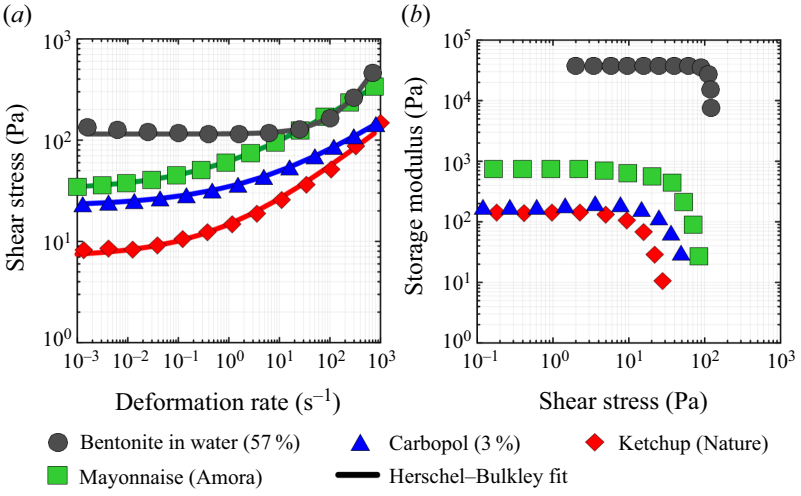

Figure 5. Rheological characterisation using an ARES-G2 rheometer (TA Instruments) equipped with a cone-plate geometry. We employ standard ramp shear tests over a range of 10^{-3} s^{-1} to 10^{3} s^{-1} to obtain stress versus deformation rate levels (*a*) in addition to oscillatory tests at 10 rad s^{-1} to obtain the storage modulus of the used fluids (*b*).

applied to the considered solenoidal flows ($\boldsymbol{\nabla} \cdot \boldsymbol{u} = 0$) reads

$$\rho\left(\frac{\partial \boldsymbol{u}}{\partial t} + \boldsymbol{u} \cdot \boldsymbol{\nabla}\boldsymbol{u} - \boldsymbol{g}\right) = -\boldsymbol{\nabla} p + \boldsymbol{\nabla} \cdot \boldsymbol{\tau} + \boldsymbol{f_{st}}, \tag{2.6}$$

in which $\boldsymbol{u}$, p, $\boldsymbol{\tau}$, $\boldsymbol{\nabla}$, $\boldsymbol{g}$, $\boldsymbol{\nabla}\cdot$ and $\boldsymbol{f_{st}}$ are, respectively, the velocity vector, the pressure, the extra-stress tensor, the gradient operator, the gravity vector, the divergence operator and a capillary term related to the surface tension force. The latter is defined as $\boldsymbol{f_{st}} = -\sigma\kappa\Phi\boldsymbol{n}$, where σ, κ, Φ and $\boldsymbol{n}$ are the surface tension, the curvature of the drop surface, the Dirac function locating the drop surface and its normal vector, respectively. In addition, the extra-stress tensor is given by $\boldsymbol{\tau} = \eta\dot{\boldsymbol{\gamma}}$, in which $\dot{\boldsymbol{\gamma}}$ represents the rate-of-strain tensor defined as $\dot{\boldsymbol{\gamma}} = (\boldsymbol{\nabla}\boldsymbol{u} + \boldsymbol{\nabla}\boldsymbol{u}^T)$. The norm of $\dot{\boldsymbol{\gamma}}$ is called the deformation rate, being defined as $|\dot{\boldsymbol{\gamma}}| = (\frac{1}{2}\dot{\boldsymbol{\gamma}} : \dot{\boldsymbol{\gamma}})^{1/2}$. The complex drop viscosity η is computed using a Herschel–Bulkley equation (Herschel & Bulkley 1926) combined with a Papanastasiou regularization (exponential parts in the following equation; Papanastasiou 1987)

$$\eta = k|\ \dot{\boldsymbol{\gamma}}\ |^{m-1}(1 - \mathrm{e}^{|-\dot{\boldsymbol{\gamma}}|/\dot{\gamma}_p})^{1-m} + \frac{\tau_0}{|\ \dot{\boldsymbol{\gamma}}\ |}(1 - \mathrm{e}^{|-\dot{\boldsymbol{\gamma}}|/\dot{\gamma}_p}), \tag{2.7}$$

where $\dot{\gamma}_p$ is the cutoff deformation rate (fixed at $\dot{\gamma}_p = 10^{-6}$ s^{-1}) that allows us to bound the value of the viscosity for vanishing $|\ \dot{\boldsymbol{\gamma}}\ |$ below $\dot{\gamma}_p$.

Our numerical methods are based on a variational multi-scale approach combined with anisotropic mesh adaptation with highly stretched elements illustrated by the black lines in figure 6(*e*) (size of the smaller mesh elements $\sim$1 μm; Riber *et al.* 2016; Valette *et al.* 2019; Pereira *et al.* 2019, 2020; Valette *et al.* 2021). The time evolution of the drop surface is captured using a level-set function (Hachem *et al.* 2016).

The 3-D numerical configuration taken into account is illustrated in figure 6(*e*), where the mesh (composed of approximately 10^6 elements) is depicted, adapted around each interface. The corresponding zero isovalues for the level-set function are also shown (in red). Four different drop initial shapes are numerically considered, as displayed in

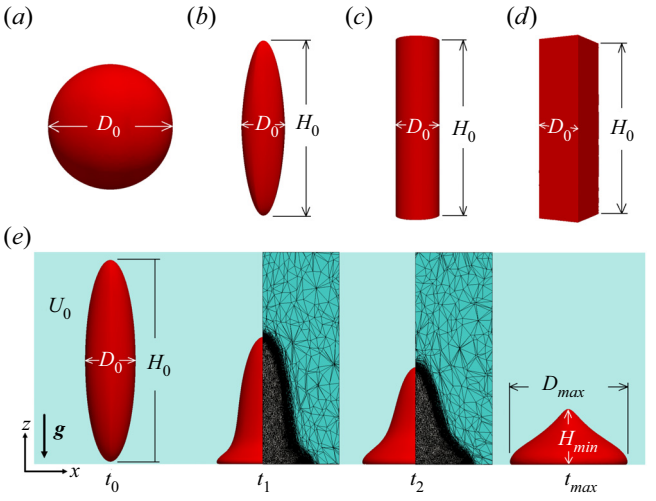

Figure 6. Four different drop initial shapes are numerically considered: (*a*) spherical, (*b*) prolate, (*c*) cylindrical and (*d*) prismatic. Their initial aspect ratio H_0/D_0 varies from 1 to 8. (*e*) Numerical configuration taken into account. The used mesh (composed of approximately 10^6 elements) adapted around each interface (viscoplastic drop in red, and air in blue) and illustrated by the black lines. The drop of height H_0 and diameter D_0 falls by gravity and hits the solid plate at the instant t_0 at an impact velocity U_0. After the impact, the drop spreads until it achieves a maximum diameter D_{max} and a minimum height H_{min} at the instant t_{max}. A movie showing a typical numerical simulation is available as a supplemental material (see supplementary movie 2; $U_0 = 1.5$ m s^{-1}, $D_0 = 3.15$ mm, $H_0 = 12.6$ mm, $\rho = 1585$ kg m^{-3}, $k = 0.1$ Pa s^m, $m = 1$, $\tau_0 = 948$ Pa).

Shape	ρ (kg m^{-3})	k (Pa s^m)	m	τ_0 (Pa)	σ (N m^{-1})	D_0 (mm)	H_0 (mm)	H_0/D_0
Spherical	500–2000	0.01–10	0.2–1	0.01–10 000	0.005–0.072	4–20	4–20	1
Prolate	500–2000	0.01–10	0.2–1	0.01–10 000	0.005–0.072	4–20	4–40	1–8
Cylindrical	500–2000	0.01–10	0.2–1	0.01–10 000	0.005–0.072	4–20	4–40	1–8
Prismatic	500–2000	0.01–10	0.2–1	0.01–10 000	0.005–0.072	4–20	4–40	1–8

Table 2. Details concerning the considered drops for the numerical simulations. Impact velocities U_0 vary from 0.5 m s^{-1} to 10 m s^{-1}.

figures 6(*a*)–6(*d*): spherical, prolate, cylindrical and prismatic. Their initial aspect ratio H_0/D_0 varies from 1 to 8. Furthermore, a wide range of drop rheological properties is explored, as detailed in table 2, while the impact velocity varies from 0.5 m s^{-1} to 10 m s^{-1}. Concerning the air phase (blue region in figure 6), both viscosity η_{air} and density ρ_{air} are constant and respectively equal to 10^{-5} Pa s and 1 kg m^{-3}. Lastly, initial and boundary conditions for the flow equations are, respectively, initial vertical impact velocity U_0 within the drop, no-slip condition between the fluids and the impacted surface (bottom plate), and zero normal stress in the other walls of the domain.

3. Results and discussions

3.1. *Spreading dynamics*

Following the analyses stressed in figure 2, supplemental aspect ratio effects are given by 3-D numerical results in figure 7. The latter shows six numerical snapshots of the

spreading process for eight viscoplastic drops at two $Re_{m,D} - Pl$ couples: $Re_{m,D} = 50$ and $Pl = 0.6$ (figure 7*a–d*; left column); and $Re_{m,D} = 150$ and $Pl = 0.07$ (figure 7*e–h*; right column). The interval Δt between two subsequent images correspond to 20 % of the necessary time to achieve the maximum spreading t_{max} ($\Delta t^* = \Delta t/t_{max} = 0.2$). The red surface in both the first and the last snapshot denotes the 3-D drop–air interface. Contours of the norm of the instantaneous velocity $|u(x, y, z, t)|$ (made dimensionless by the maximum instantaneous velocity $|u_{max}(t)|$) on the centre x–z plane are represented on the left side of the second through fifth snapshot of each displayed case. Yielded (flowing; $|\boldsymbol{\tau}| > \tau_0$; black) and unyielded (non-flowing; $|\boldsymbol{\tau}| \leq \tau_0$; grey) regions are illustrated on their right side. During the spreading process, the drops develop shear flow within the yielded regions as a result of the no-slip interactions between the solid surface and the viscoplastic material. The more $Re_{m,D}$ increases and Pl decreases (moving from the left-column results to the right-column ones), the more the drops behave like a liquid and spread. Note also that for a fixed $Re_{m,D} - Pl$, (i) viscoplastic drops with different volumes but equal aspect ratios exhibit the same spreading dynamics (velocity field, yielded/unyielded regions and maximum relative spreading); and (ii) viscoplastic drops with distinct aspect ratios present contrasting spreading dynamics even when they exhibit the same volume, as observed by comparing figure 7(*b*) to figure 7(*d*), and/or figure 7(*f*) to figure 7(*h*). Additionally, the volume of unyielded regions is accentuated by the increase of H_0/D_0. More specifically, high aspect ratio drops tend to preserve their upper portion (solid-like portion), while their bottom part spreads like a liquid, dissipating the kinetic energy. Such a deformation localisation within the bottom portion of the material naturally leads to D_{max}/D_0 levels greater than those observed for smaller aspect ratio objects impacting at the same $Re_{m,D} - Pl$. Hence, D_{max}/D_0 appears as an increasing function of H_0/D_0. Obviously, once the kinetic energy is completely dissipated ($|u(x, y, z, t)| = 0\ \mathrm{m\ s^{-1}}$), the whole drop behaves like a solid, as highlighted by the grey region in the last snapshot of each case.

Aspect ratio effects are equally observed when considering the height-based Reynolds number $Re_{m,H}$. In figure 8, six numerical snapshots illustrate the time evolution of spherical (figure 8*a*) and prolate drops (figure 8*b*,*c*) impacting at $Re_{m,H} = 150$ and $Pl = 0.07$. As in figure 7, contours of the norm of the instantaneous velocity $|u(x, y, z, t)|$ (made dimensionless by the maximum instantaneous velocity $|u_{max}(t)|$) on the centre x–z plane are represented on the left side of the second through fifth snapshot of each displayed case. Yielded (flowing; black) and unyielded (non-flowing; grey) regions are displayed on their right side. As observed by comparing figures 8(*a*) and 8(*c*), drops sharing the same volume but a distinct aspect ratio exhibit different velocity field, yielded/unyielded regions and maximum relative spreading. However, at a fixed aspect ratio, the drops present the same impact dynamics, regardless of their volume, as seen by examining figures 8(*b*) and 8(*c*).

Further aspect ratio effects are underlined by figure 9, in which the instantaneous volume fraction of unyielded regions $V_{unyielded}/V_{total} \times 100[\%]$ is plotted as a function of t/t_{max} for spherical (open symbols) and prolate numerical objects ($H_0/D_0 = 4$; solid symbols). Subfigures are related to $Re_{m,D} - Pl$ couples: $Re_{m,D} = 50$ and $Pl = 0.6$ (figure 9*a*); $Re_{m,D} = 150$ and $Pl = 0.07$ (figure 9*b*); $Re_{m,H} = 150$ and $Pl = 0.07$ (figure 9*c*). Additionally, each symbol form (circle, triangle and diamond) indicates a specific drop volume V_{total}. Inset plots stressing the minimum $V_{unyielded}/V_{total}$ are also provided. At a fixed $Re_{m,D} - Pl$, drops with a similar aspect ratio exhibit equal $V_{unyielded}/V_{total}$ curves, regardless of their volume. Moreover, in each subfigure $V_{unyielded}/V_{total}$ appears as an increasing function of H_0/D_0. Such a result emerges from the fact that the augmentation

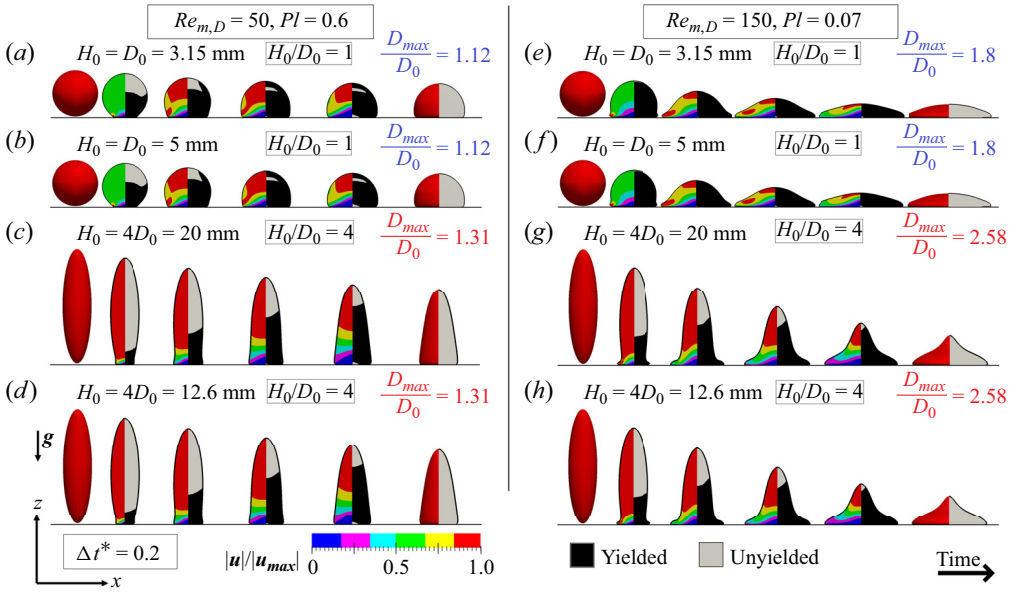

Figure 7. Six numerical snapshots of the spreading process for eight viscoplastic drops at two $Re_{m,D} - Pl$ couples: $Re_{m,D} = 50$ and $Pl = 0.6$ (figure 7*a–d*; left column); $Re_{m,D} = 150$ and $Pl = 0.07$ (figure 7*e–h*; right column). The interval Δt between two subsequent images corresponds to 20 % of the necessary time to achieve the maximum spreading t_{max} ($\Delta t^* = \Delta t/t_{max} = 0.2$). The drop volumes, their aspect ratio and their maximum relative spreading are respectively: (*a*) $V_{total} = 1.64 \times 10^{-8}$ m^3, $H_0/D_0 = 1$, $D_{max}/D_0 = 1.12$; (*b*) $V_{total} = 6.54 \times 10^{-8}$ m^3, $H_0/D_0 = 1$, $D_{max}/D_0 = 1.12$; (*c*) $V_{total} = 2.62 \times 10^{-7}$ m^3, $H_0/D_0 = 4$, $D_{max}/D_0 = 1.31$; (*d*) $V_{total} = 6.54 \times 10^{-8}$ m^3, $H_0/D_0 = 4$, $D_{max}/D_0 = 1.31$; (*e*) $V_{total} = 1.64 \times 10^{-8}$ m^3, $H_0/D_0 = 1$, $D_{max}/D_0 = 1.8$; (*f*) $V_{total} = 6.54 \times 10^{-8}$ m^3, $H_0/D_0 = 1$, $D_{max}/D_0 = 1.8$; (*g*) $V_{total} = 2.62 \times 10^{-7}$ m^3, $H_0/D_0 = 4$, $D_{max}/D_0 = 2.58$; (*h*) $V_{total} = 6.54 \times 10^{-8}$ m^3, $H_0/D_0 = 4$, $D_{max}/D_0 = 2.58$. The red surface in both the first and the last snapshot indicates the 3-D drop–air interface. Contours of the norm of the instantaneous velocity $|u(x, y, z, t)|$ (made dimensionless by the maximum instantaneous velocity $|u_{max}(t)|$) on the centre x–z plane are represented on the left side of the second through fifth snapshot of each displayed case. Yielded (flowing; $|\boldsymbol{\tau}| > \tau_0$; black) and unyielded (non-flowing; $|\boldsymbol{\tau}| \leq \tau_0$; grey) regions are illustrated on their right side.

of H_0/D_0 leads to a deformation localisation within the bottom part of the drop, while its upper part tends to remain unyielded. In the opposite sense, the increase of $Re_{m,D}$ and the decrease of Pl favour the fluidization of the drop, as observed by examining figures 9(*a*) and 9(*b*). Hence, the drops tend to behave like a liquid when their impacting inertial stress increases with respect of the viscoplastic one.

Another interesting aspect ratio effect is shown by figure 10, where the instantaneous relative diameter $D(t)/D_0$ is plotted as a function of t/t_{max} for spherical (figure 10*a*) and prolate drops with $H_0/D_0 = 4$ (figure 10*b*) and $H_0/D_0 = 8$ (figure 10*c*). Their volume is fixed at $V_{total} = 2.62 \times 10^{-7}$ m^3. In each subfigure, three $Re_{m,D} - Pl$ couples are explored: $Re_{m,D} = 80$ and $Pl = 0.002$ (grey circles); $Re_{m,D} = 80$ and $Pl = 0.03$ (blue triangles); and $Re_{m,D} = 80$ and $Pl = 0.7$ (red diamonds). First, at a constant aspect ratio, the drop spreading is mitigated by the increment of Pl. Additionally, the enlargement of H_0/D_0 leads to higher D_{max}/D_0 levels at a fixed $Re_{m,D} - Pl$ couple (compare, for instance, the grey circle curves in figures 10*a*, 10*b* and 10*c*). However, this effect tends to vanish when plasticity increases and, consequently, the drop tends to behave like a solid (note that the red diamond curves are close to one another, while the grey circle curves exhibit very different relative spreading levels). Hence, drops impacting at higher Pl are less exposed

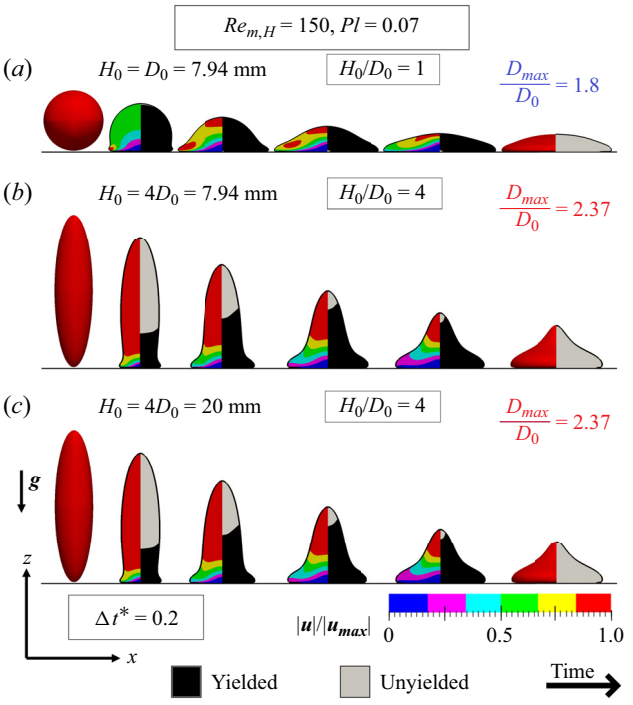

Figure 8. Six numerical snaphots obtained at $Re_{m,H} = 150$ and $Pl = 0.07$ illustrate the spreading evolution of spherical and prolate drops: (*a*) $V_{total} = 2.62 \times 10^{-7}$ m^3, $H_0/D_0 = 1$, $D_{max}/D_0 = 1.8$; (*b*) $V_{total} = 1.64 \times 10^{-8}$ m^3, $H_0/D_0 = 4$, $D_{max}/D_0 = 2.37$; (*c*) $V_{total} = 2.62 \times 10^{-7}$ m^3, $H_0/D_0 = 4$, $D_{max}/D_0 = 2.37$. The red surface in both the first and the last snapshot indicates the 3-D drop–air interface. Contours of the norm of the instantaneous velocity $|u(x, y, z, t)|$ (made dimensionless by the maximum instantaneous velocity $|u_{max}(t)|$) on the centre x–z plane are represented on the left side of the second through fifth snapshot of each displayed case. Yielded (flowing; black) and unyielded (non-flowing; grey) regions are illustrated on their right side.

to aspect ratio effects than those hitting the solid plate at Pl close to 0 (fully viscous scenario).

3.2. *Energy transfer analyses*

Aiming to highlight the physical mechanism driving the aspect ratio effects presented above, we carry out energy budget analyses. More specifically, in figure 11, energy percentage curves are plotted as a function of t/t_{max}: kinetic energy (blue triangles), surface energy (grey circles), gravitational energy (green squares) and dissipation (red diamonds). The latter is divided into two parts: viscous dissipation (orange triangles) and plastic dissipation (black asterisks). These terms are defined as $KE = (1/2)\int_V \rho|\boldsymbol{u}|^2\,\mathrm{d}V$ (kinetic energy), $SE = \int_S \sigma\,\mathrm{d}S$ (surface energy), $G = \int_V \rho g z\,\mathrm{d}V$ (gravitational energy), $W = \int_t \int_V k|\dot{\boldsymbol{\gamma}}|^{m+1} + \tau_0|\dot{\boldsymbol{\gamma}}|\,\mathrm{d}V\,\mathrm{d}t$ (dissipation), $W_m = \int_t \int_V k|\dot{\boldsymbol{\gamma}}|^{m+1}\,\mathrm{d}V\,\mathrm{d}t$ (viscous dissipation) and $W_{\tau_0} = \int_t \int_V \tau_0|\dot{\boldsymbol{\gamma}}|\,\mathrm{d}V\,\mathrm{d}t$ (plastic dissipation), where V and S denote the drop volume and surface, respectively (similar to Sanjay, Lohse & Jalaal 2021; Valette *et al.* 2021). Each computed energy term is made dimensionless by the total energy of the system ($= KE(t = t_0) + SE(t = t_0) + G(t = t_0) + W(t = t_0)$) and generically represented by variable ε^*. Aspect ratio effects on the spreading dynamics are stressed using four different numerical drops: $H_0/D_0 = 1$ and $V_{total} = 6.54 \times 10^{-8}$ m^3

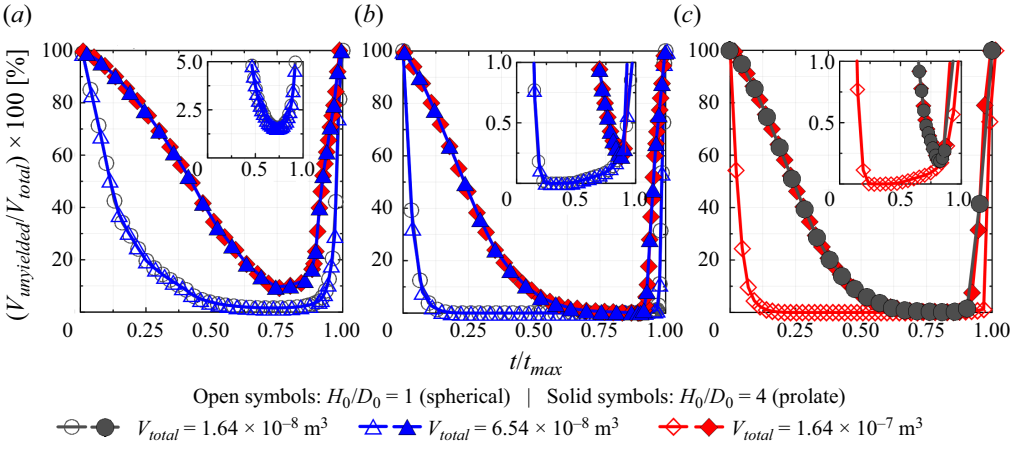

Figure 9. Instantaneous volume fraction of unyielded regions $V_{unyielded}/V_{total} \times 100[\%]$ plotted as a function of dimensionless time t/t_{max} for spherical (open symbols) and prolate numerical objects ($H_0/D_0 = 4$; solid symbols). For each subfigure, both the Reynolds number and the plastic number are kept fixed: (*a*) $Re_{m,D} = 50$ and $Pl = 0.6$, (*b*) $Re_{m,D} = 150$ and $Pl = 0.07$, and (*c*) $Re_{m,H} = 150$ and $Pl = 0.07$. Each symbol form indicates a specific drop volume V_{total}: $V_{total} = 1.64 \times 10^{-8}$ m^3 (circles); $V_{total} = 6.54 \times 10^{-8}$ m^3 (triangles); $V_{total} = 1.64 \times 10^{-7}$ m^3 (diamonds). Inset plots stressing the minimum $V_{unyielded}/V_{total}$ are also provided.

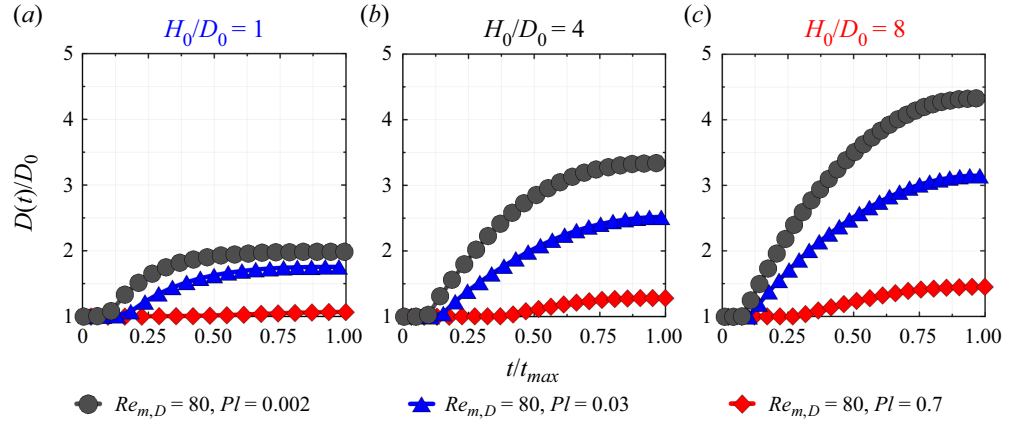

Figure 10. Instantaneous relative diameter $D(t)/D_0$ as a function of dimensionless time t/t_{max} for spherical (*a*) and prolate numerical drops at $H_0/D_0 = 4$ (*b*) and $H_0/D_0 = 8$ (*c*). Their volume is fixed at $V_{total} = 2.62 \times 10^{-7}$ m^3. In each subfigure, three $Re_{m,D} - Pl$ couples are explored: $Re_{m,D} = 80$ and $Pl = 0.002$ (grey circles), $Re_{m,D} = 80$ and $Pl = 0.03$ (blue triangles), and $Re_{m,D} = 80$ and $Pl = 0.7$ (red diamonds).

(first line); $H_0/D_0 = 1$ and $V_{total} = 2.62 \times 10^{-7}$ m^3 (second line); $H_0/D_0 = 4$ and $V_{total} = 2.62 \times 10^{-7}$ m^3 (third line); and $H_0/D_0 = 4$ and $V_{total} = 6.54 \times 10^{-8}$m^3 (fourth line). For each one of them, three $Re_{m,D} - Pl$ couples are considered: $Re_{m,D} = 112.5$ and $Pl = 0.002$ (*a*,*d*,*g*,*j*); $Re_{m,D} = 112.5$ and $Pl = 0.05$ (*b*,*e*,*h*,*k*); and $Re_{m,D} = 112.5$ and $Pl = 0.5$ (*c*,*f*,*i*,*l*).

For all 12 impact events displayed in figure 11, the drop kinetic energy is primarily dissipated during its spreading (note that both the surface energy and the gravitational one play a marginal role in comparison to the other energy terms, as mentioned in § 2).

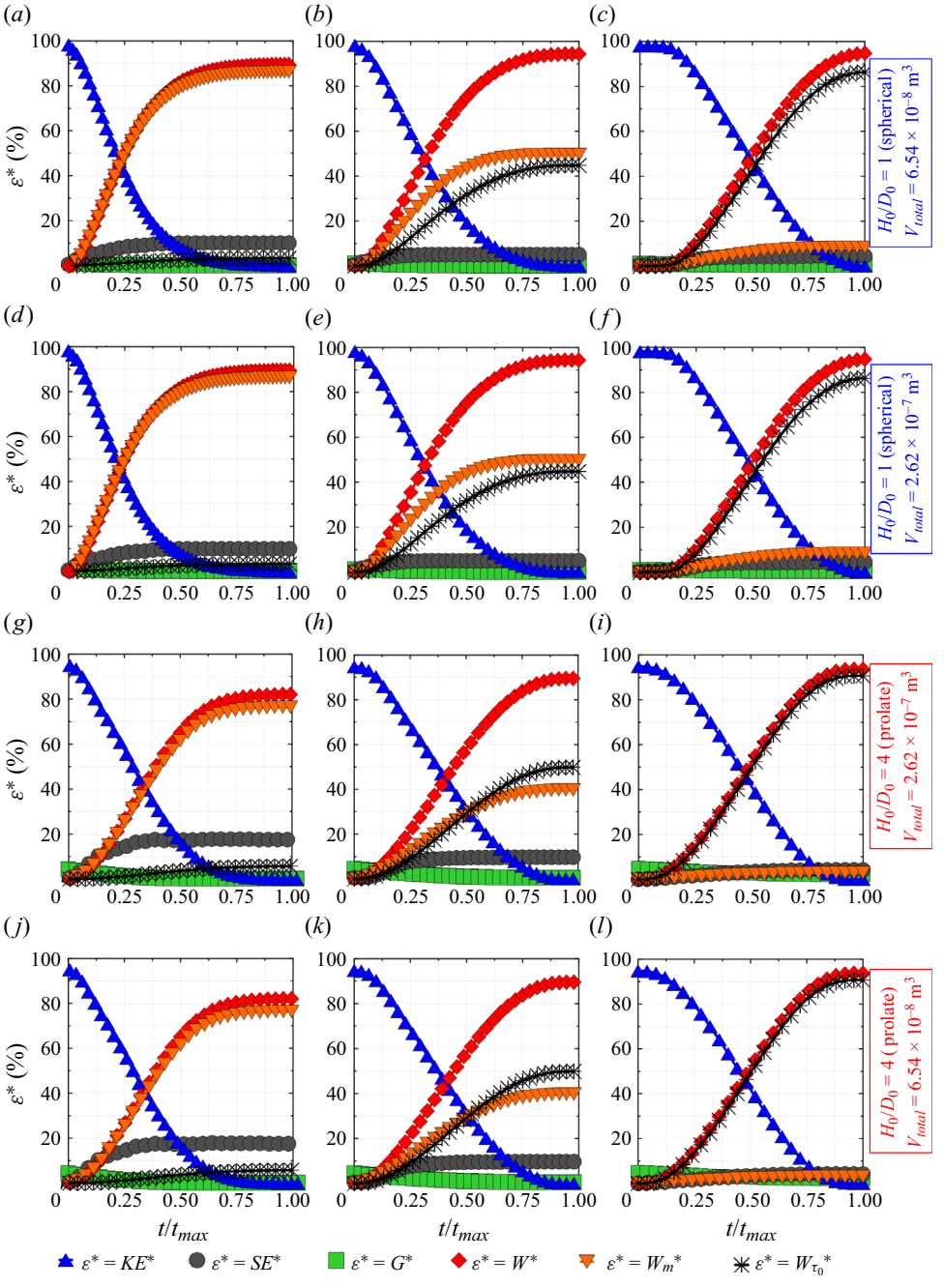

Figure 11. Energy percentage curves plotted as a function of dimensionless time t/t_{max}: kinetic energy (blue triangles), surface energy (grey circles), gravitational energy (green squares) and dissipation (red diamonds). The latter is divided into two parts: viscous dissipation (orange triangles) and plastic dissipation (black asterisks). The computed terms are made dimensionless by the total energy of the system and generically represented by variable ε^*. Aspect ratio effects on the spreading dynamics are pointed out with the aid of four different numerical drops: $H_0/D_0 = 1$ and $V_{total} = 6.54 \times 10^{-8}$ m^3 (first line); $H_0/D_0 = 1$ and $V_{total} = 2.62 \times 10^{-7}$ m^3 (second line); $H_0/D_0 = 4$ and $V_{total} = 2.62 \times 10^{-7}$ m^3 (third line); and $H_0/D_0 = 4$ and $V_{total} = 6.54 \times 10^{-8}$m^3 (fourth line). For each of them, three $Re_{m,D} - Pl$ couples are considered: $Re_{m,D} = 112.5$ and $Pl = 0.002$ (a,d,g,j); $Re_{m,D} = 112.5$ and $Pl = 0.05$ (b,e,h,k); and $Re_{m,D} = 112.5$ and $Pl = 0.5$ (c,f,i,l).

Nevertheless, the dissipative process exhibits particular signatures depending on $Re_{m,D}$, Pl and H_0/D_0. For the drops impacting at $Re_{m,D} = 112.5$ and $Pl = 0.002$, for example, plasticity is negligible and, consequently, dissipation is basically driven by the viscous stress ($k|\dot{\boldsymbol{\gamma}}|^m$). However, when increasing Pl to 0.05 and keeping $Re_{m,D}$ and H_0/D_0 fixed (middle-column results), plastic dissipation becomes comparable to the viscous one ($\tau_0|\dot{\boldsymbol{\gamma}}| \approx k|\dot{\boldsymbol{\gamma}}|^{m+1}$). Interestingly, the former becomes slightly dominant by increasing H_0/D_0 from 1 (spherical) to 4 (prolate), as highlighted by opposing the middle-column results above and below the black horizontal line. Such a result is rather in line with the augmentation of the unyielded volume fraction induced by the increase of aspect ratio exposed in figure 9. It clearly indicates that the shape of the drop affects the dissipative mechanism during the spreading. Logically, plastic effects are strengthened by the increase of Pl, eventually leading to a plasticity-driven dissipation, as shown by the third-column results. Lastly, it is worth noting that the volume of the drop does not affect the energy percentage curves displayed in figure 11, which can be observed by comparing the top-line curves with the second-line ones (and/or the third-line with the fourth-line curves) at fixed $Re_{m,D}$ and Pl.

Supplemental energy transfer analyses are conducted in figures 12 and 13, respectively, for spherical and $H_0/D_0 = 4$ prolate numerical drops with the same volume $V_{total} = 2.62 \times 10^{-7}$ m^3. Each subfigure is related to a specific $Re_{m,D} - Pl$ couple: $Re_{m,D} = 112.5$ and $Pl = 0.002$ (figures 12*a* and 13*a*); $Re_{m,D} = 112.5$ and $Pl = 0.05$ (figures 12*b* and 13*b*); and $Re_{m,D} = 112.5$ and $Pl = 0.5$ (figures 12*c* and 13*c*). They are composed of six upper-line snapshots and six bottom-line snapshots ($\Delta t^* = t/t_{max} = 0.2$). The first one shows the 3-D drop–air interface in red. From the second to the last upper-line snapshot, $|\dot{\boldsymbol{\gamma}}|/(U_0/H_0)$ contours are displayed on the left side of the centre x–z plane, while yielded (black) and unyielded (grey) regions are shown on the right side. Furthermore, from the second to the last bottom-line snapshot, the dissipative process is stressed by $k|\dot{\boldsymbol{\gamma}}|^{m+1}/(\rho U_0^3/H_0)$ and $\tau_0|\dot{\boldsymbol{\gamma}}|/(\rho U_0^3/H_0)$ contours on the left and right side of the centre x–z plane, respectively. Logically, greater dissipation levels are observed within high deformation rate zones developed at the vicinities of the solid substrate due to the imposed no-slip condition. As Pl moves from 0.002 to 0.5, dissipation switches from a viscous-dominated process to a plastic-dominated one, and tends to occur exclusively in the bottom portion of the drop, where the shear stresses overpass τ_0. Such a localisation effect is also favoured by the augmentation of H_0/D_0 (figure 13*b*,*c*), since shear stresses tend to vanish far from the wall (in the upper portion of the drops) for any impact event. Note, for example, that more than 50 % of the prolate drop shown by the second snapshot in figure 13(*a*) exhibits a very low deformation rate (blue contour) against less than 25 % for the spherical drop displayed by the corresponding snapshot in figure 12(*a*). It is equally important to emphasise that the vicinities of the interfaces between yielded (liquid-like) and unyielded (solid-like) zones are characterised by low deformation rate levels, which naturally makes them plasticity-driven from a dissipative standpoint (plastic dissipation is proportional to $|\dot{\boldsymbol{\gamma}}|$, whereas viscous dissipation is comparable to $|\dot{\boldsymbol{\gamma}}|^{m+1}$). Hence, the growth of such interfaces induced by the increase of H_0/D_0 may lead to a swelling of the plastic dissipation, as observed by comparing spherical to prolate energy curves at a fixed $Re_{m,D} - Pl$ couple in figure 11. Lastly, despite the differences observed at low and high Pl, it is worth noting that, from an average viewpoint, the height of the dissipative layer remains comparable to H_{min}, as pointed out by the magenta dashed line in figures 12(*b*) and 13(*b*). For this reason, H_{min} is used to estimate the mean viscous dissipation in the following subsection.

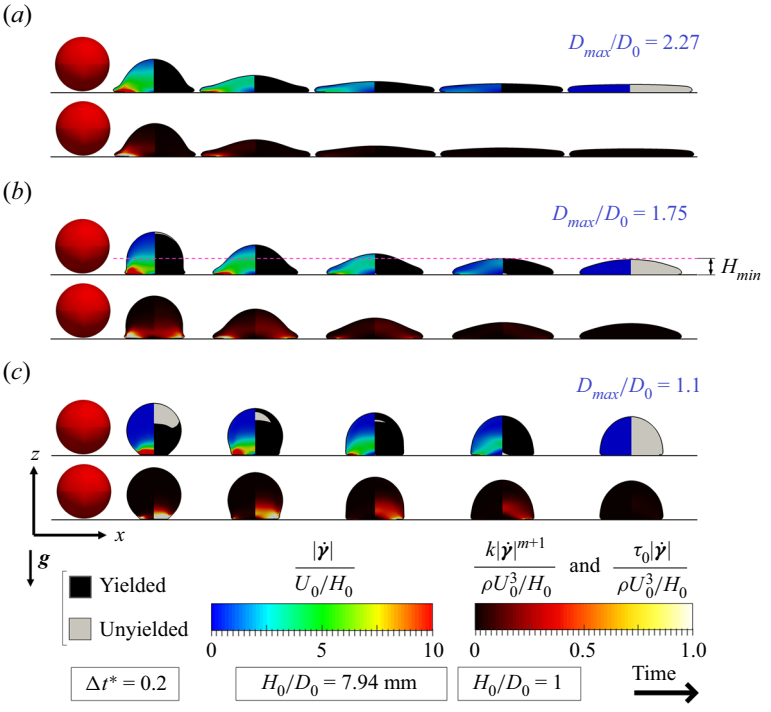

Figure 12. Spherical numerical drops ($H_0/D_0 = 1$) with the same volume $V_{total} = 2.62 \times 10^{-7}$ m^3. Each subfigure is related to a specific $Re_{m,D} - Pl$ couple: (*a*) $Re_{m,D} = 112.5$ and $Pl = 0.002$; (*b*) $Re_{m,D} = 112.5$ and $Pl = 0.05$; (*c*) $Re_{m,D} = 112.5$ and $Pl = 0.5$. They are composed of six upper-line snapshots and six bottom-line snapshots ($\Delta t^* = t/t_{max} = 0.2$). The first one shows the 3-D drop–air interface in red. From the second to the last upper-line snapshot, $|\dot{\boldsymbol{\gamma}}|/(U_0/H_0)$ contours are displayed on the left side of the centre x–z plane, while yielded (black) and unyielded (grey) regions are shown on the right side. Additionally, from the second to the last bottom-line snapshot, the dissipative process is stressed by $k|\dot{\boldsymbol{\gamma}}|^{m+1}/(\rho U_0^3/H_0)$ and $\tau_0|\dot{\boldsymbol{\gamma}}|/(\rho U_0^3/H_0)$ contours on the left and right side of the centre x–z plane, respectively.

3.3. *Scaling laws: maximum spreading, spreading time, minimum height and final shape*

Based on the energy transfer analyses conducted above, we propose scaling laws for D_{max} by considering at least two spreading regimes: inertio-viscous (figure 11*a*,*d*,*g*,*j*) and inertio-plastic (figure 11*c*,*f*,*i*,*l*). The scaling laws are developed in the following paragraph.

In the inertio-viscous spreading regime, the impacting kinetic energy of the drop ($\sim \rho U_0^2 H_0 D_0^2$) is primarily dissipated by viscous effects ($\sim k(U_c/H_{min})^m D_{max}^3$, where U_c represents a characteristic dissipation velocity, which will be approximated, at first glance, as U_0). On the other hand, in the inertio-plastic spreading regime, the kinetic energy is mainly dissipated by plastic effects ($\sim \tau_0 D_{max}^3$). Together with mass conservation ($H_0 D_0^2 \sim H_{min} D_{max}^2$), we conclude that D_{max}/D_0 scales as $[Re_{m,D}(H_0/D_0)^{m+1}]^{1/2m+3}$ in the former scenario and $[(1/Pl)(H_0/D_0)]^{1/3}$ in the latter. For the inertio-viscous scaling, aspect ratio effects on D_{max}/D_0 are amplified by the growth of $Re_{m,D}$. However, for the inertio-plastic scaling, the drop spreading becomes less exposed to aspect ratio effects as Pl increases. Such tendencies are rather in line with the results brought up by figure 10. It is also worth noting that when working with spherical drops ($H_0/D_0 = 1$) we recover scaling laws previously reported in the literature (Luu & Forterre 2009), i.e. ${Re_{m,D}}^{1/2m+3}$ (inertio-viscous spreading) and $(1/Pl)^{1/3}$ (inertio-plastic spreading).

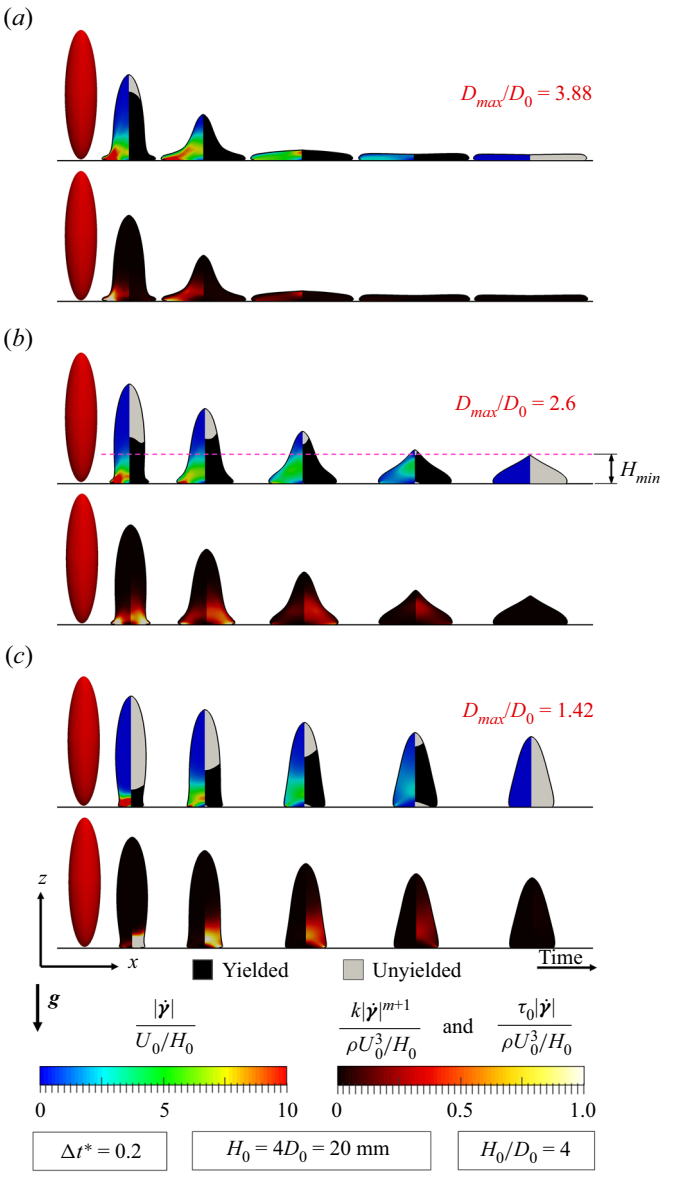

Figure 13. Prolate numerical drops ($H_0/D_0 = 4$) with the same volume $V_{total} = 2.62 \times 10^{-7}$ m^3. Subfigures are related to specific $Re_{m,D} - Pl$ couples: (*a*) $Re_{m,D} = 112.5$ and $Pl = 0.002$; (*b*) $Re_{m,D} = 112.5$ and $Pl = 0.05$; (*c*) $Re_{m,D} = 112.5$ and $Pl = 0.5$. They are composed of six upper-line snapshots and six bottom-line snapshots ($\Delta t^* = t/t_{max} = 0.2$). The first snapshot shows the 3-D drop–air interface in red. From the second to the last upper-line snapshot, $|\dot{\boldsymbol{\gamma}}|/(U_0/H_0)$ contours are displayed on the left side of the centre x–z plane, while yielded (black) and unyielded (grey) regions are shown on the right side. Additionally, from the second to the last bottom-line snapshot, the dissipative process is stressed by $k|\dot{\boldsymbol{\gamma}}|^{m+1}/(\rho U_0^3/H_0)$ and $\tau_0|\dot{\boldsymbol{\gamma}}|/(\rho U_0^3/H_0)$ contours on the left and right side of the centre x–z plane, respectively.

Moreover, for Newtonian spherical drops, m is equal to 1, and so $D_{max}/D_0 \sim Re_{m,D}{}^{1/5}$, as widely cited in the literature (Clanet *et al.* 2004; Laan *et al.* 2014; Josserand & Thoroddsen 2016; Wildeman *et al.* 2016).

By equating the scaling laws presented above, we define the impact number $I = (1/Pl)^{1/3}(1/Re_{m,D})^{1/2m+3}(H_0/D_0)^{-m/6m+9} = 1$, a unifying dimensionless parameter for both the inertio-plastic and the inertio-viscous spreading that approaches to 1 at the transition between the mentioned regimes. In other words, regime transition is expected to occur at $I \approx 1$.

The validity of the above theoretical arguments is corroborated by figure 14, in which the rescaled maximum spreading $(D_{max}/D_0)/[Re_{m,D}(H_0/D_0)^{m+1}]^{1/2m+3}$ is plotted as a function of I not only for spherical, prolate, cylindrical and prismatic numerical objects but also for spherical and non-spherical experimental drops (asterisks; error bars are comparable to the size of the symbols). More specifically, in figure 14(*a*) the results are plotted using the impact number definition given by Luu & Forterre (2009), $(1/Pl)^{1/3}(1/Re_{m,D})^{1/2m+3}$, while in figure 14(*b*) the impact number developed in the present work is used. Comparing these subfigures, we clearly note that, when the aspect ratio effects are taken into account, the points collapse across a single path divided into three regions linked with three spreading regimes: inertio-plastic (I; $I \leq 1$; blue box); the inertio-viscous (II; $I \geq 3$; red box); and a mixed regime (III; $1 < I < 3$; white box), for which inertial, viscous and plastic effects all play an important role (the viscous dissipation is comparable to the plastic one). The mixed inertio-visco-plastic region is defined based on the detachment of the points from both the inertio-plastic scaling (black dash-dotted line) and the inertio-viscous one (black dotted line). Interestingly, for the impact number interval explored here ($0.2 \leq I \leq 100$), the results can be fitted by the following Padé approximant (polynomial expression)

$$P = 0.9\frac{I^3 + I^2 + I}{I^3 + I^2 + I + 1}, \tag{3.1}$$

which in turn is represented by the red line in figure 14(*b*). Padé approximants similar to that given in (3.1) are typically employed in drop impact works to represent master curves (Laan *et al.* 2014; Josserand & Thoroddsen 2016). Hence, D_{max}/D_0 can be predicted by the following equation:

$$\frac{D_{max}}{D_0} = P\left[\left(\frac{H_0}{D_0}\right)^{m+1} Re_{m,D}\right]^{1/2m+3}. \tag{3.2}$$

Additionally, thanks to the mass conservation ($\sqrt{H_0/H_{min}} \sim D_{max}/D_0$), we can plot the rescaled minimum height $\sqrt{H_0/H_{min}}/[Re_{m,D}(H_0/D_0)^{m+1}]^{1/2m+3}$ as a function of the impact number, as illustrated in figure 14(*c*). Once again, the points collapse across a single path divided into the three regimes mentioned previously (only numerical results related to prolate drops are shown, for clarity). In inertio-plastic impact events the upper part of the drop tends to preserve its initial shape, while its bottom portion spreads radially. As a result, prolate impacting objects exhibit a more conical shape at the end of the spreading process, as illustrated by the blue drop (see also figures 2*c* and 13*c*). However, as plastic effects are attenuated, and consequently I increases, the drop final shape becomes flattened (pancake-like, in red), which characterises inertio-viscous impact events (see figures 4*b* and 13*a*).

It is important to underline that, as observed by examining figure 14(*a*) with figure 14(*b*), the augmentation of H_0/D_0 can induce an increase of more than 80 % in D_{max}/D_0, in respect to spherical objects. Additionally, although shape effects on the impact number stay relatively low even for the highest aspect ratio drop considered here (<15 % for $H_0/D_0 = 8$), they can eventually lead to spreading regime changes, especially for impact

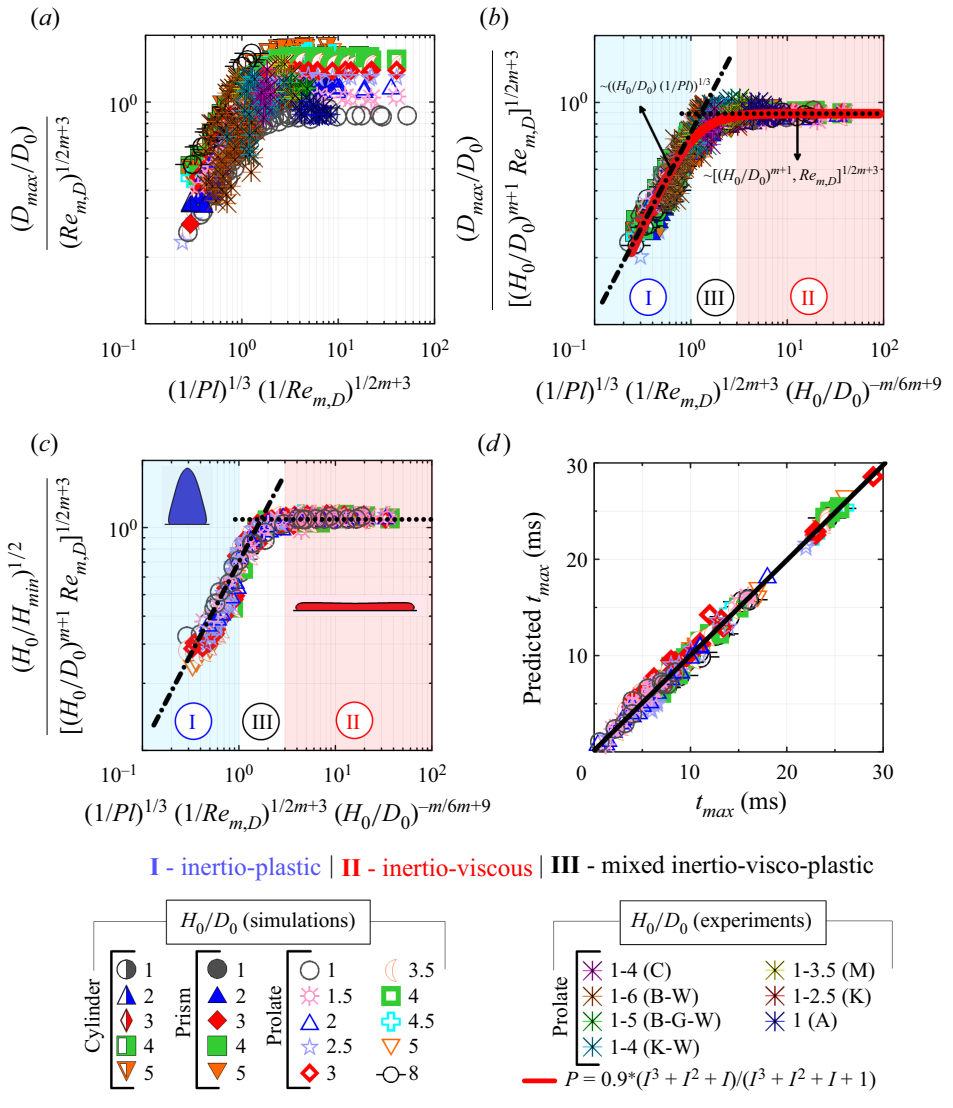

Figure 14. (*a*) Rescaled maximum spreading plotted using the scaling laws and the impact number definition given by Luu & Forterre (2009): $(D_{max}/D_0)/[Re_{m,D}]^{1/2m+3}$ against $(1/Pl)^{1/3}(1/Re_{m,D})^{1/2m+3}$. (*b*) Rescaled maximum spreading plotted using the scaling laws and the impact number definition taking the drop aspect ratio into account (present work): $(D_{max}/D_0)/[Re_{m,D}(H_0/D_0)^{m+1}]^{1/2m+3}$ against $(1/Pl)^{1/3}(1/Re_{m,D})^{1/2m+3}(H_0/D_0)^{-m/6m+9}$. The symbols denote aspect ratio values (for the numerical simulations) or intervals (for the experiments; asterisks). (*c*) Rescaled minimum height as a function of the impact number (only numerical results related to prolate drops are plotted, for clarity). (*d*) Comparisons between the spreading time t_{max} obtained from numerical simulations using prolate drops, and the one predicted by combining (3.4) and (3.2).

events at I close to 1 and/or 3 (critical values giving the interfaces between the three impact zones illustrated in figure 14*b*,*c*). Hence, the role of drop shape in the impact/spreading process cannot be overestimated.

Lastly, an expression for the drop maximum spreading time is proposed through energy conservation arguments, by considering both the viscous and the plastic source of energy

dissipation, i.e.

$$\rho U_0^2 H_0 D_0^2 \sim k(U_c/H_{min})^m D_{max}^3 + \tau_0 D_{max}^3. \tag{3.3}$$

By defining the spreading time $t_{max} = D_{max}/U_c$, and together with mass conservation ($H_0 D_0^2 \sim H_{min} D_{max}^2$), we find that

$$t_{max} = \left[\frac{Ak \left(\frac{D_{max}}{D_0}\right)^{3m+3} \left(\frac{D_0}{H_0}\right)^{m+1}}{B\rho U_0^2 - C\tau_0 \left(\frac{D_0}{H_0}\right) \left(\frac{D_{max}}{D_0}\right)^3} \right]^{1/m}, \tag{3.4}$$

where A, B and C are adjustable prefactors, and D_{max}/D_0 can be approximated as $P[Re_{m,D}(H_0/D_0)^{m+1}]^{1/2m+3}$ according to (3.2), ultimately giving us a predicted t_{max}. The latter is plotted against the measured t_{max} in figure 14(*d*) for a wide range of H_0/D_0 with $A = 1.25$, $B = 0.4$ and $C = 1$ (for clarity, only numerical results are shown). As observed, both the predicted and the measured spreading time are in good agreement with each other.

In short, figure 14 emphasises that the viscoplastic drop-spreading dynamics is deeply affected by H_0/D_0, which in turn reveals the potential of using drop shape to control spreading.

4. Concluding remarks and perspectives

In this paper we have experimentally and numerically studied the normal impact of viscoplastic drops on a solid plate under negligible capillary effects. We have extended the seminal work reported by Luu & Forterre (2009) by highlighting the fundamental role of shape in the normal impact of viscoplastic drops. In this connection, spherical, prolate, cylindrical and prismatic drops have been analysed and their rheological behaviour was expressed through a classical Herschel–Bulkley constitutive equation. Supplemental non-Newtonian signatures such as microstructural orientation/anisotropy and thixotropy have not been considered.

High aspect ratio viscoplastic drops tend to preserve their upper portion (solid-like portion), while their bottom part spreads like a liquid, dissipating the kinetic energy. Such a deformation localisation within the bottom portion of the material naturally leads to D_{max}/D_0 levels greater than those observed for smaller aspect ratio objects impacting at the same $Re_{m,D} - Pl$. Hence, D_{max}/D_0 appears as an increasing function of H_0/D_0.

In short, results show that the drop impacting kinetic energy is primarily dissipated through viscoplastic effects during the spreading process, giving rise to three flow regimes: (i) inertio-viscous (balancing kinetic and viscous stresses); (ii) inertio-plastic (balancing the kinetic stress and yield stress); and (iii) mixed inertio-visco-plastic (balancing kinetic and viscoplastic stresses). They are highly affected by the initial aspect ratio of the drop, and can be found using the impact number $I = (1/Pl)^{1/3}(1/Re_{m,D})^{1/2m+3}(H_0/D_0)^{-m/6m+9}$. The drop maximum spreading, minimum height, spreading time and final shape are all directly linked with the impact number as well.

Our study has direct applications in a number of impact-based situations, which includes spraying generation, firefighting, inkjet printing, atomization, viscoplastic water entry and 3-D printing of organs, tissues, prosthetics and electronic components, among others (Modak *et al.* 2020; Murphy & Atala 2020; Vijayavenkataraman *et al.* 2018; Jalaal *et al.* 2019; Lorenceau & Quéré 2003; Bordoloi & Longmire 2014; Ryu *et al.* 2017;

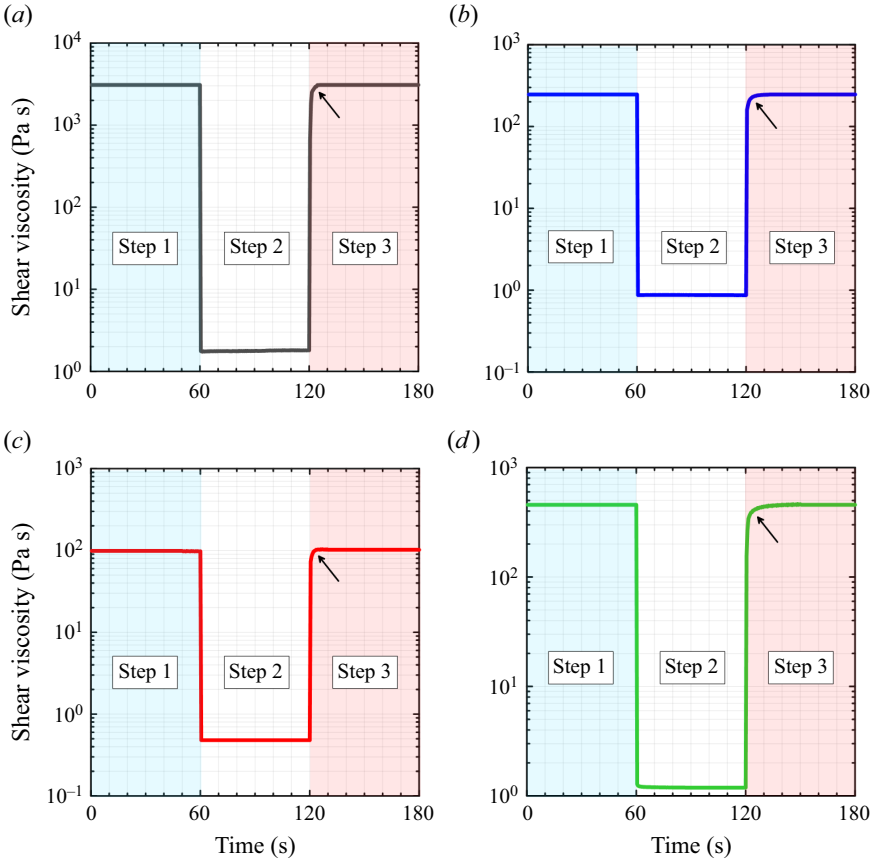

Figure 15. Three-step deformation rate rheological tests: 57 % bentonite (*a*), 3 % Carbopol (*b*), 'Nature' ketchup (*c*) and 'Amora' mayonnaise (*d*). These tests were carried out using an ARES-G2 rheometer (TA Instruments) equipped with a cone-plate geometry. At each step, the shear viscosity is plotted as a function of time (over 60 s) at a specific deformation rate: 0.1 s^{-1} at steps 1 and 3; and 100 s^{-1} at step 2. The black arrows indicate the recovery process.

Kumar *et al.* 2018; Soto *et al.* 2018; Su *et al.* 2020). More specifically, the mentioned applications could benefit from the diagrams highlighted in figure 14, which ultimately could be used to predict and control the spreading dynamics (spreading time, maximum spreading, minimum height and final shapes) of prolate viscoplastic drops impacting on a solid surface (in purely viscoplastic scenarios).

Finally, in terms of perspectives, since complex fluids are highly diffused in industrial domains, it would be interesting to consider in future works supplemental non-Newtonian effects on the spreading dynamics, such as those related to elasticity and/or thixotropy. Similar analyses using bentonite suspensions at lower concentrations (<50 % and, consequently, $k \approx 0.01$ Pa s^m and $\tau_0 < 50$ Pa) would be welcome as well since they could be used to explore supplemental spreading regimes balanced by the inertial stress, the capillary pressure and the yield stress.

Supplementary movies. Supplementary movies are available at https://doi.org/10.1017/jfm.2023.926.

Acknowledgements. We would like to thank Mrs C. Borgo for her great help with some of the experiments performed here, as well as Professor C. Ligoure (University of Montpellier) and Dr L. Ramos (University of Montpellier) for fruitful discussions.

Funding. The authors also would like to acknowledge the support from the UCA^{JEDI} program (IDEX of Université Côte d'Azur), the PSL Research University under the program 'Investissements d'Avenir' launched by the French government and implemented by the French National Research Agency (ANR) with the reference ANR-10-IDEX-0001-02 PSL, and the ANR for supporting the INNpact project under the 'Jeunes chercheuses et jeunes chercheurs' program.

Declaration of interests. The authors report no conflict of interest.

Author ORCIDs.
Rudy Valette https://orcid.org/0000-0002-1779-7453;
Anselmo Pereira https://orcid.org/0000-0001-6688-1013.

Appendix. Thixotropy

Aiming to underline thixotropic effects, we present in figure 15 three-step deformation rate rheological tests for the samples shown in figure 5: 57 % bentonite (figure 15*a*), 3 % Carbopol (figure 15*b*), 'Nature' ketchup (figure 15*c*) and 'Amora' mayonnaise (figure 15*d*). These tests were carried out using an ARES-G2 rheometer (TA Instruments) equipped with a cone-plate geometry. At each step, the shear viscosity is plotted as a function of time (over 60 s) at a specific deformation rate: 0.1 s^{-1} at steps 1 and 3; and 100 s^{-1} at step 2. An acquisition rate of 10 points per second was chosen. As observed, thixotropic recovery time scales $t_{thixotropy}$ vary from $O(10^0)$ s (figure 15*a–c*) to $O(10^1)$ s (figure 15*d*), which is at least 100 times longer than the analysed impact events ($t_{max} \approx O(10^{-2})$ s). Hence, thixotropic effects have not been considered in our theoretical analyses. Nevertheless, since $t_{thixotropy} \gg t_{max}$, future numerical studies focusing on both the local and time evolution of the breakdown/recovery process during the drop spreading would be more than welcome.

References

Andrade, R., Osorio, F. & Skurtys, O. 2013 Drop impact behavior on food using spray coating: fundamentals and applications. *Food Res. Intl* **54**, 397–405.

Balmforth, N.J., Frigaard, I. & Ovarlez, G. 2014 Yielding to stress: recent developments in viscoplastic fluid mechanics. *Annu. Rev. Fluid Mech.* **46**, 121–146.

Balmforth, N.J., Forterre, Y. & Pouliquen, O. 2009 The viscoplastic Stokes layer. *J. Non-Newtonian Fluid Mech.* **158**, 46–53.

Blackwell, B.C., Deetjen, M.E., Gaudio, J.E. & Ewoldt, R.H. 2015 Sticking and splashing in yield-stress fluid drop impacts on coated surfaces. *Phys. Fluids* **27**, 043101.

Bonn, D., Eggers, J., Indekeu, J., Meunier, J. & Rolley, E. 2009 Wetting and spreading. *Rev. Mod. Phys.* **81**, 739.

Bordoloi, A.D. & Longmire, E.K. 2014 Drop motion through a confining orifice. *J. Fluid Mech.* **759**, 520–545.

Bottiglieri, P., de Sio, F., Fasanaro, G., Mojoli, G., Impembo, M. & Castaldo, D. 1991 Rheological characterization of ketchup. *J. Food Quality* **14**, 497–512.

Carlson, A., Do-Quang, M. & Amberg, G. 2011 Dissipation in rapid dynamic wetting. *J. Fluid Mech.* **682**, 213–240.

Chafe, N.P. & Bruyn, J.R. 2005 Drag and relaxation in a bentonite clay suspension. *J. Non-Newtonian Fluid Mech.* **131**, 44–52.

Chun, B., Kwon, I., Jung, H.W. & Hyun, J.C. 2017 Lattice Boltzmann simulation of shear-induced particle migration in plane Couette–Poiseuille flow: local ordering of suspension. *Phys. Fluids* **29**, 121605.

Clanet, C., Béguin, C., Richard, D. & Quéré, D. 2004 Maximal deformation of an impacting drop. *J. Fluid Mech.* **517**, 199–208.

Cohen-Addad, S., Reinhard, H. & Pitois, O. 2013 Flow in foams and flowing foams. *Annu. Rev. Fluid Mech.* **45**, 241–267.

Coupez, T. & Hachem, E. 2013 Solution of high-Reynolds incompressible flow with stabilized finite element and adaptive anisotropic meshing. *Comput. Meth. Appl. Mech. Engng* **267**, 65–85.

Coussot, P. 2005 *Rheometry of Pastes, Suspensions and Granular Materials*. Wiley Interscience.

COUSSOT, P. 2007 Rheophysics of pastes: a review of microscopic modelling approaches. *Soft Matt.* **3**, 528–540.

COUSSOT, P. & GAULARD, F. 2005 Gravity flow instability of viscoplastic materials: the ketchup drip. *Phys. Rev.* E **72** (031409), 1–5.

COUSSOT, P., ROUSSEL, N., JARNY, S. & CHANSON, H. 2005 Continuous or catastrophic solid–liquid transition in jammed systems. *Phys. Fluids* **17**, 011704.

DAGES, N., LIDON, P., PIGNON, F., MANNEVILLE, S. & GIBAUD, T. 2021 Mechanics and structure of carbon black gels under high-power ultrasound. *J. Rheol.* **65**, 477–490.

DERKACH, S.R. 2009 Rheology of emulsions. *Adv. Colloid Interface Sci.* **151**, 1–23.

DUEZ, C., YBERT, C., CLANET, C. & BOCQUET, L. 2010 Wetting controls separation of inertial flows from solid surfaces. *Phys. Rev. Lett.* **104**, 084503.

DE GENNES, P.-G., BROCHARD-WYART, F. & QUÉRÉ, D. 2005 *Gouttes, Bulles, Perles et Ondes*. Belin.

GERMAN, G. & BERTOLA, V. 2009 Impact of shear-thinning and yield-stress drops on solid substrates. *J. Phys.: Condens. Matter* **21**, 1–16.

GODEFROID, J. 2019 Complex fluids dripped into a liquid bath: impact, relaxation and gelation dynamics. PhD thesis, ESPCI Paris.

GUAZZELLI, E. & POULIQUEN, O. 2018 Rheology of dense granular suspensions. *J. Fluid Mech.* **852**, 1–61.

HACHEM, E., KHALLOUFI, M., BRUCHON, J., VALETTE, R. & MESRI, Y. 2016 Unified adaptive variational multiscale method for two phase compressible and incompressible flows. *Comput. Meth. Appl. Mech. Engng* **308**, 238–255.

HERSCHEL, V.W.H. & BULKLEY, R. 1926 Konsistenz-messungen von gummi-benzollosungen. *Kolloidn. Z.* **39**, 291–300.

JALAAL, M., KEMPER, D. & LOHSE, D. 2019 Viscoplastic water entry. *J. Fluid Mech.* **864**, 596–613.

JØRGENSEN, L., FORTERRE, Y. & LHUISSIER, H. 2020 Deformation upon impact of a concentrated suspension drop. *J. Fluid Mech.* **896**, 1–11.

JOSSERAND, C. & THORODDSEN, S.T. 2016 Drop impact on a solid surface. *Annu. Rev. Fluid Mech.* **48**, 365–391.

KIM, E. & BAEK, J. 2012 Numerical study of the parameters governing the impact dynamics of yield-stress fluid droplets on a solid surface. *J. Non-Newtonian Fluid Mech.* **173–174**, 62–71.

KOOCHEKI, A., GHANDI, A., RAZAVI, S.M.A., MORTAZAVI, S.A. & VASILJEVIC, T. 2009 The rheological properties of ketchup as a function of different hydrocolloids and temperature. *Intl J. Food Sci. Technol.* **44**, 596–602.

KUMAR, A., TRIPATHY, A., NAM, Y., LEE, C. & SEN, P. 2018 Effect of geometrical parameters on rebound of impacting droplets on leaky superhydrophobic meshes. *Soft Matt.* **14**, 1571–1580.

LAAN, N., DE BRUIN, K.G., BARTOLO, D., JOSSERAND, C. & BONN, D. 2014 Maximum diameter of impacting liquid droplets. *Phys. Rev. Appl.* **2**, 044018.

LIN, Y., ZHU, H., WANG, W., CHEN, J., PHAN-THIEN, N. & PAN, D. 2019 Rheological behavior for laponite and bentonite suspensions in shear flow. *J. Food Quality* **14**, 125233.

LIU, Q., LO, J.H.Y., LI, U., LIU, Y., ZHAO, J. & XU, L. 2021 The role of drop shape in impact and splash. *Nat. Commun.* **12**, 1–8.

LOISEL, V., ABBAS, M., MASBERNAT, O. & CLIMENT, E. 2015 Inertia-driven particle migration and mixing in a wall-bounded laminar suspension flow. *Phys. Fluids* **27**, 123304.

LORENCEAU, E. & QUÉRÉ, D. 2003 Drops impacting a sieve. *J. Colloid Interface Sci.* **263**, 244–249.

LUU, L.-H. & FORTERRE, Y. 2009 Drop impact of yield-stress fluids. *J. Fluid Mech.* **632**, 301–327.

LUU, L.-H. & FORTERRE, Y. 2014 Giant drag reduction in complex fluid drops on rough hydrophobic surfaces. *Phys. Rev. Lett.* **110**, 184501.

MA, M. & BARBOSA-CÁNOVAS, G.V. 1995*a* Rheological characterization of mayonnaise. Part I: slippage at different oil and xanthan gum concentrations. *J. Food Engng* **25**, 397–408.

MA, M. & BARBOSA-CÁNOVAS, G.V. 1995*b* Rheological characterization of mayonnaise. Part II: flow and viscoelastic properties at different oil and xanthan gum concentrations. *J. Food Engng* **25**, 409–425.

MODAK, C.D., KUMAR, A., TRIPATHY, A. & SEN, P. 2020 Drop impact printing. *Nat. Commun.* **11**, 1–11.

MURPHY, S.V. & ATALA, A. 2020 3D bioprinting of tissues and organs. *Nat. Biotechnol.* **32**, 773–785.

MWASAME, P.M., WAGNER, N.J. & BERIS, A.N. 2016 Modeling the viscosity of polydisperse suspensions: improvements in prediction of limiting behavior. *Phys. Fluids* **28**, 061701.

NESS, C., SETO, R. & MARI, R. 2022 The physics of dense suspensions. *Annu. Rev. Condens. Matter Phys.* **13**, 97–117.

NIGEN, S. 2005 Experimental investigation of the impact of an (apparent) yield-stress material. *Atomiz. Sprays* **15**, 103–117.

OISHI, C.M., THOMPSON, R.L. & MARTINS, F.P. 2019 Normal and oblique drop impact of yield stress fluids with thixotropic effects. *J. Fluid Mech.* **876**, 642–679.
PAIU, J.-M. 2007 Carbopol gels: elastoviscoplastic and slippery glasses made of individual swollen sponges; meso-and macroscopic properties, constitutive equations and scaling laws. *J. Non-Newtonian Fluid Mech.* **144**, 1–29.
PAPANASTASIOU, T.C. 1987 Flows of materials with yield. *J. Rheol.* **31**, 385–404.
PEREIRA, A., HACHEM, E. & VALETTE, R. 2020 Inertia-dominated coiling instabilities of power-law fluids. *J. Non-Newtonian Fluid Mech.* **282**, 104321.
PEREIRA, A., LARCHER, A., HACHEM, E. & VALETTE, R. 2019 Capillary, viscous, and geometrical effects on the buckling of power-law fluid filaments under compression stresses. *Comput. Fluids* **190**, 514–519.
PETERS, I.R., XU, Q. & JAEGER, H.M. 2013 Splashing onset in dense suspension droplets. *Phys. Rev. Lett.* **111**, 028301.
PIGNON, F., MAGNIN, A. & PIAU, J.-M. 1996 Thixotropic colloidal suspensions and flow curves with minimum: identification of flow regimes and rheometric consequences. *J. Rheol.* **40**, 573–587.
QUÉRÉ, D. 2008 Wetting and roughness. *Annu. Rev. Fluid Mech.* **38**, 71–99.
QUETZERI-SANTIAGO, M.A., YOKOI, K., CASTREJON-PITA, A.A. & CASTREJON-PITA, R. 2019 Role of the dynamic contact angle on splashing. *Phys. Rev. Lett.* **122**, 1–6.
REIN, M. 1993 Phenomena of liquid drop impact on solid and liquid surfaces. *Fluid Dyn. Res.* **12**, 61–93.
RIBER, S., VALETTE, R., MESRI, Y. & HACHEM, E. 2016 Adaptive variational multiscale method for Bingham flows. *Comput. Fluids* **138**, 51–60.
RICHARD, D., CLANET, C. & QUÉRÉ, D. 2002 Contact time of a bouncing drop. *Nature* **417**, 811.
RYU, S., SEN, P., NAM, Y. & LEE, C. 2017 Water penetration through a superhydrophobic mesh during a drop impact. *Phys. Rev. Lett.* **118**, 14501.
SANJAY, V., LOHSE, D. & JALAAL, M. 2021 Bursting bubble in a viscoplastic medium. *J. Fluid Mech.* **922**, A2.
SEN, S., MORALES, A.G. & EWOLDT, R.H. 2020 Viscoplastic drop impact on thin films. *J. Fluid Mech.* **891**, A27.
SOTO, D., GIRARD, H.-L., LE HELLOCO, A., BINDER, T., QUÉRÉ, D. & VARANASI, K.K. 2018 Droplet fragmentation using a mesh. *Phys. Rev. Fluids* **3**, 083602.
SU, M.-J., LUO, Y., CHU, G.-W., CAI, Y., LE, Y., ZHANG, L.-L. & CHEN, J.-F. 2020 Dispersion behaviors of droplet impacting on wire mesh and process intensification by surface micro/nano-structure. *Chem. Engng Sci.* **219**, 1–13.
TANNER, R.I. 2018 Review article: aspects of non-colloidal suspension rheology. *Phys. Fluids* **30**, 101301.
TENORIO-GARCIA, A., ARAIZA-CALAHORRA, A., SIMONE, E. & SARKAR, A. 2022 Recent advances in design and stability of double emulsions: trends in pickering stabilization. *Food Hydrocolloid* **128**, 107601.
THOMPSON, R.L., SICA, L.U.R. & DE SOUZA MENDES, P.R. 2018 The yield stress tensor. *J. Non-Newtonian Fluid Mech.* **261**, 211–219.
THOMPSON, R.L. & SOARES, E.J. 2016 Viscoplastic dimensionless numbers. *J. Non-Newtonian Fluid Mech.* **238**, 57–64.
VALETTE, R., HACHEM, E., KHALLOUFI, M., PEREIRA, A.S., MACKLEY, M.R. & BUTLER, S.A. 2019 The effect of viscosity, yield stress, and surface tension on the deformation and breakup profiles of fluid filaments stretched at very high velocities. *J. Non-Newtonian Fluid Mech.* **263**, 130–139.
VALETTE, R., PEREIRA, A., RIBER, S., SARDO, L., LARCHER, A. & HACHEM, E. 2021 Viscoplastic dam-breaks. *J. Non-Newtonian Fluid Mech.* **287**, 1–21.
VÁZQUEZ-QUESADA, A. & ELLERO, M. 2016 Analytical solution for the lubrication force between two spheres in a bi-viscous fluid. *Phys. Fluids* **28**, 073101.
VIJAYAVENKATARAMAN, S., YAN, W.-C., LU, W.F., WANG, C.-H. & FUH, J.Y.H. 2018 3D bioprinting of tissues and organs for regenerative medicine. *Adv. Drug Deliv. Rev.* **132**, 296–332.
WILDEMAN, S., VISSER, C.W., SUN, C. & LOHSE, D. 2016 On the spreading of impacting drops. *J. Fluid Mech.* **805**, 636–655.
WORTHINGTON, A.M. 1883 On impact with a liquid surface. *Proc. R. Soc. Lond.* **34**, 217–230.
YARIN, A.L. 2006 Drop impact dynamics: splashing, spreading, receding, bouncing.... *Annu. Rev. Fluid Mech.* **38**, 159–192.
YUMOTO, M., HEMMI, N., SATO, N., KAWASHIMA, Y., ARIKAWA, K., IDE, K., HOSOKAWA, M., SEO, M. & TAKEYAMA, H. 2020 Evaluation of the effects of cell-dispensing using an inkjet-based bioprinter on cell integrity by RNA-seq analysis. *Sci. Rep.* **10**, 1–10.
ZHANG, H.P. & MAKSE, H.A. 2005 Jamming transition in emulsions and granular materials. *Phys. Rev.* E **72**, 011301.